ABSTRACT

Title of Thesis: THE EFFECTS OF TEMPERATURE AND SURFACTANTS ON SECONDARY DROPLETS GENERATED BY THE IMPACT OF RAINDROPS ON A WATER SURFACE

Xiguang Zhang
Master of Science, 2023

Thesis Directed by: Professor James H. Duncan
Professor Xinan Liu
Department of Mechanical Engineering
University of Maryland

The effects of temperature and surfactant on secondary droplets produced by the impact of raindrops on water surface were experimentally studied in a rain facility that consists of a rain generator and a deep water pool. The rain generator is a 0.9 m $\times$ 0.6 m rectangular tank with 360 hypodermic needles mounted on its bottom. A constant water height is maintained in the tank to obtain a constant dripping rate of raindrops from the needles. The rain generator is placed 2.2 meters above the water pool that is 1.22 m long by 1.22 m wide with a water depth of 0.31 m. A circular motion of the rain generator varies the impact locations of the raindrops on the water surface.

Both the raindrops and secondary droplets are measured with an in-line holographic technique that employs a collimated laser beam and a high-speed camera. The diameters and two-dimensional positions of the raindrops and secondary droplets were first reconstructed in each holographic

image using a GPU-based holographic reconstruction algorithm. Then an in-house particle tracking code was implemented to compute their diameters, trajectories and instantaneous velocities. The measurement data shown in this thesis was taken at 9.5 cm above the water surface of the pool.

In this study, the effects of temperature and surface tension on the production of the secondary droplets were examined separately. When studying the temperature effect, the temperature of the water in the rain generator varied from 7 degrees Celsius to 20 degrees Celsius (room temperature) while the water temperature in the pool was maintained at room temperature. When studying the surface tension effect, certain amounts of soluble surfactant (Triton X-100) was added into the water pool to vary the surface tension from 40 mN/m to 73 mN/m, while the rain water is kept clean with a surface tension of 73 mN/m.

It is found that both the rain temperature and the surface tension of the water pool have an impact on the production of secondary droplets. The temperature of the rain could change the viscosity by more than 40%, therefore resulting in a significant difference in the number and the size distribution of the production of secondary droplets. On the other hand, while the surface tension of the water pool does not heavily influence the number of secondary droplets, it does contribute to a difference in size distributions of these droplets at around R = 120 μm.

THE EFFECTS OF TEMPERATURE AND SURFACTANTS ON SECONDARY DROPLETS GENERATED BY THE IMPACT OF RAINDROPS ON A WATER SURFACE

by

Xiguang Zhang

Thesis submitted to the Faculty of the Graduate School of the
University of Maryland, College Park in partial fulfillment
of the requirements for the degree of
Master of Science
2023

Advisory Committee:
Professor James H. Duncan, Chair/Advisor
Professor Xinan Liu, Advisor
Professor Kenneth T. Kiger

Dedication

To my family.

Acknowledgments

I want to express my gratitude to all the people who have made my research and this thesis possible, and my graduate experience wouldn't be complete without any one of you.

First and the most important overall, I want to thank my advisor and mentor, professor James H. Duncan. His knowledge and experience has helped me countless times during my graduate study, and his patience and personality also affected me for the long term to become a better person. I appreciate everything he has done for me both on the academic aspect as well as on my life.

I would also like to express my appreciation to my supporter and mentor professor Xinan Liu. His theoretical ideas has guided me throughout my research, and I have gained many valuable experimental skills from him. He has been a huge help during my graduate study by making himself always available to my endless questions, and it was such a great experience and an honorable opportunity to work with him.

I want to say thank you to all the co-workers at Hydrodynamic laboratory who have provided many help on my experiment whenever needed. Professor Kenneth Kiger has spent his valuable time being my committee member and provided critical comments. Dr. Martin Erinin has guided me through some of the earliest stages of the research. Dr. An Wang and Samuel Lee have provided me many other angles when I got stuck on a specific problem. Winnie, Sophia and I had many small relaxing conversations in between some of the boring times during the research.

Special thank you to Dr. Chang Liu. He has involved in almost every part of my experiment study. We have spent many memorable time together on and off campus, in and out of the work. He has been supportive about every decision I make, and at the same time he was always able to provide constrictive suggestions for the questions I ask. He has been my closest friend during the two years of study.

I would like to acknowledge the financial support from the National Science Foundation (NSF), Division of Ocean Science, for the project discussed in the following thesis.

I also would like to mention everyone who have helped me on anything in my life. It is hard to remember all of your names and please forgive me if I did not mention you in this section. Every one of you is important for me.

Table of Contents

List of Tables

List of Figures

Chapter 1: Introduction

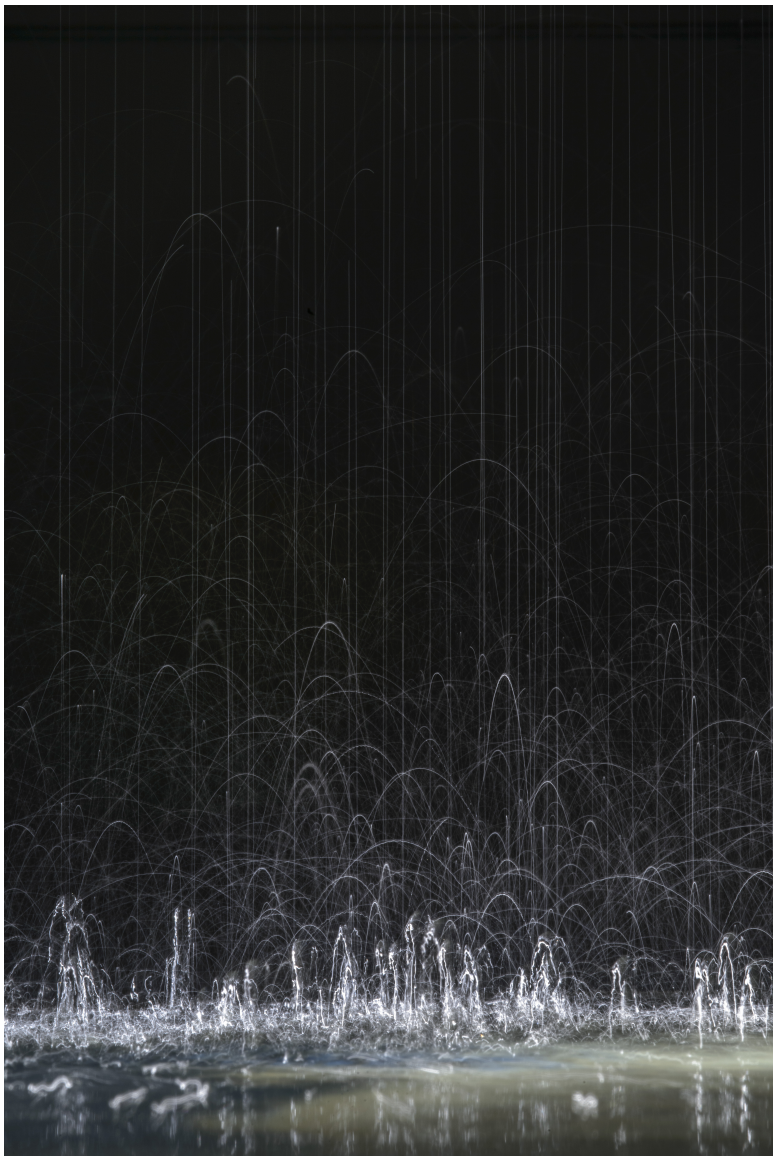

Figure 1.1: Long Exposure Photo of Rain Field

In our laboratory experiment, we captured a fascinating scene depicted in Figure 1.1. This image showcases a long exposure photo, revealing distinct vertical trails formed by raindrops. Additionally, the lower half of the image displays a noticeable layer of secondary droplets. Notably, the larger secondary droplets tend to gather closer to the water surface, while some manage to traverse a remarkable distance, reaching the topmost region of the image, sometimes covering three times the distance. The presence of this droplet layer introduces intricate effects on both the atmosphere and the radar signal. Therefore, it is of utmost importance to comprehend their behavior thoroughly.

1.1 Background and Motivation

Rainfall is a fundamental component of the Earth's water cycle, and it plays a crucial role in sustaining life on our planet. It has a significant impact on the exchange of heat, mass, and momentum between the atmosphere and the ocean. Latent heat, which accounts for about 80% of the global atmospheric heat energy, is released during precipitation, thereby influencing this exchange process [7]. Interestingly, the ocean receives approximately 79% of the total global precipitation, enhancing mass transfer across the air-water interface [8, 9]. So it is important for us to study every aspect of rainfall over the ocean.

However, our knowledge about marine precipitation is limited due to technical difficulties and poorly deployed measurement equipment. Traditional methods to estimate rain intensity and frequency of rainstorms include rain gauges and ground-based radars. However, accurately determining the spatial extent of a rainstorm on the ocean remains difficult with these methods. To address this issue, spaceborne radar systems have been employed to visualize the footprint

of rain cells on the ocean's surface [10, 11], such as the precipitation radar aboard the U.S.-Japanese Tropical Rainfall Measuring Mission satellite [7]. These sensors reveal circular or oval bright patterns with distinct edges, representing the rain cells. However, the fine-scale features generated by the rain on the ocean surface significantly influence the appearance of these patterns, which remains an active research topic (discussed further in the subsequent section).In many radar images, there are black spots located at the center of these bright patterns. Atlas [10] proposed that these bright patterns are a result of cool downdrafts accompanying the rain that reach the surface, diverging to generate winds and surface waves that can be detected by the radar. Moreover, Atlas speculated that the echo-free hole, or black spot, at the center of the rain cells is due to the damping of short waves by intense rainfall. Conversely, Lin et al. [12] argued that the echo-free hole is a consequence of the attenuation of radar signals by rain drops in the atmosphere. Unfortunately, due to the complexity of this phenomenon and the associated measurement challenges, field experiments have yet to provide conclusive data to resolve these issues.

When a drop hits the water surface, it creates a splash that consists of several components. These include a crown, which is the edge of the circular crater formed by the impact; a stalk, which is the local rebound of the water surface in response to the impact; and secondary drops and ring waves that propagate outward due to gravity and surface tension. Past studies has shown the importance of the stalk and the ring waves. However, there is no complete study on the characteristics of the secondary droplet generated by rain field and yet it also plays an important role during the rainfall process.

Droplets are commonly observed in the oceans, lakes and seas. These droplets make significant contributions to the exchange of the momentum, heat, mass and moisture between

the atmosphere and the oceans [1, 2, 13]. Previous studies showed that sea spray have significant impact on weather, such as it could increase the intensity of tropical cyclone through the exchange of enthalpy and momentum [5, 6]. Moreover, sea spray can enhance certain chemical reactions near the air-sea interface, and sea spray aerosol can serve as a reactive medium in the atmosphere, transforming chemical reactions [14, 15].

1.2 Previous Research

Figure 1.2a shows a close-up photograph of a single drop impacting a still water surface with an impact angle of 90°. A perfect horizontal stalk was generated during this event. At the base of the stalk, we could also see ring wave being generated during the impact. This event has been studied extensively in the past thirty years due to its repeatability and its simplicity. In comparison Figure 1.2b shows what actually happens during our experiment. A very chaotic and turbulent surface profile is constantly changing, causing a varying impact angle which could be visualized from irregular stalk shapes. In the air, we could see secondary droplets that are generated with different size. All the phenomena have made the research difficult and rare.

The generation of complex surface features associated with raindrop impact on a deep water pool is a crucial aspect of ocean rain processes. These features include crowns, stalks, secondary droplets, ring waves, and turbulence beneath the water surface. Because the impacts of raindrops are random in both space and time, the surface features in response to each individual raindrop vary considerably. Simple investigations of this phenomenon, such as examining the impact of a single drop on a calm water surface, have been underway for more than a century, as illustrated by the work of Reynolds, Worthington, Stow, and others [16, 17, 19]. In addition, Rein [18]'s review

(a) (b)

Figure 1.2: White Light Close-Up Photo: Fig (a) shows a stalk and ring waves during single drop impact event, Fig (b) shows chaotic behavior during impact in the rain field, stalk and secondary droplets are clearly visible.

provides extensive information on the phenomenon of single drop impact in a very organized way.

1.2.1 Single Drop Impact

The impact of a single drop on a still liquid surface gives rise to a range of phenomena. Initially, the surface of the liquid pool is forced downward, creating a depression at the point of impact and a surrounding rim of displaced liquid that forms a crown. This is followed by the release of small droplets, known as secondary droplets, from the top of the crown. Subsequently, the crown retracts, and the depression rebounds, generating a liquid jet, or stalk, at the center of the crater. Depending on the conditions of impact, droplets may also form at the tip of the stalk, referred to as tip drops. Moreover, surface waves, also known as ring waves, are generated due to the oscillation of the liquid surface caused by the impact. Additionally, a single drop

impact produces vortex rings that penetrate further down into the liquid pool, adding to the list of phenomena observed.

One important dimensionless variable involved in the drop impact event is Weber number, and it is calculated by:

$$We = \frac{\rho V^2 D}{ST} \tag{1.1}$$

where ρ is the density of the liquid, V is the impact velocity, D is the diameter of the drop, and ST is the surface tension of the target liquid. Both Stow and Liu [19, 20]'s paper reported a strong relationship of the secondary droplet characteristic with Weber number.

Worthington [17] has studied and wrote extensively about splash characteristics produced from single drop in his book. He used high speed photography technique to capture different phenomenons happened during the drop impact with more than 100 illustrations including low-fall, higher-fall, impact with different liquid, and even impact with solid sphere. The water drop impact onto water is especially reviewed here since its relevancy to my experiment. Worthington has included all the figures that he has taken in all the experiments to give us a rough understanding of different types of splash production mechanism in single drop impact events.

Stow [19] has studied the size distribution of the secondary droplet production. His group experimentally studied secondary droplet production from single drop event with different drop diameter and impacting velocity. The target surface of their experiment including both liquid and solid. They have tried multiple droplet detection methods including dye-on-filter-paper, dye-in-water, dye-on-slide and finally decided to use photographic emulsion technique. The size distribution that they have reported to be a log-normal distribution with different parameters

depending on different cases. Number of secondary droplet production when drop impact a medium rough surface is also predicted.

Liu's group [20] has studied closer in single drop impact on 2010, with constant drop number and varying impact velocity, impact angle, and ambient pressure experimentally. They have developed a theoretical Kelvin-Helmholtz instability model that helps explaining the splash phenomenon including gas motion around the impacting droplet. They have studied very closely on the small scale features that happens during the impact event on the spreading velocity and splash angle due to the effect of Weber number, ambient pressure and the impacting angle. They have also developed a simulation model to compare with the experimental data and was able to get a large-ranged threshold on the three factors.

Alghoul [21] has studied the event when a drop impacting a up-moving liquid film. The impact Weber number is varied between 0.6 and 460, the Renolds number of the target liquid film is between 351 to 1818, and the film height is varied between 4.3mm and 9.4 mm. The different impacting features due to different conditions were reported in the article.

Several experiments have been conducted to investigate the impact of droplets on pre-disturbed wavy surfaces. In one study, Schotland [22] and Jayaratne and Mason [23] examined the effects of droplet impacts on surfaces previously disturbed by impacts. The results showed that the impact-induced surface features were minimally affected by the pre-existing surface waves. However, the impact frequency used in these experiments was low, and the liquid layer surface may have mostly recovered from the previous impact.

In contrast, Siscoe and Levin [24] studied the interaction between surface waves and impacting drops under high frequency impact conditions. They accomplished this by allowing a continuous sequence of drops to fall onto a water surface contained in a circular battery jar. The battery

jar walls would reflect waves generated by previous drops back to the center to interact with the following drops. When the drops fell at a constant frequency, a steady state would emerge, in which each drop impacted the surface wave at a fixed phase. The phase could be adjusted by changing the drop rate, the initial drop height, and the battery jar's diameter. The researchers found that, depending on whether the drop hit the crest or trough of the wave, it would either be absorbed and amplify the surface wave or generate an unusually high stalk, respectively. They also observed that the impact-induced vortex rings and eddies were confined to a depth of roughly 5 to 10 cm.

1.2.2 Raindrops Impacting a Deep Liquid Pool

The complexity of raindrop impacts on a liquid pool increases significantly when considering the physical process as a whole, rather than just a single drop. The interaction between a specific raindrop and the pool's surface is influenced by the random distribution of previous and concurrent raindrop impacts, which affects the free surface movements and subsurface flow characteristics. Various phenomena linked to raindrop impacts on liquid pools have been investigated, such as the creation of rain-induced stalks, surface waves, and sub-surface turbulence.

In contrast to the extensive research on single drop impacts, only a limited number of articles address the generation of rain-induced stalks and their behavior in a rain field. Wetzel [25] reported on the distribution of stalk heights in two rain fields with similar rates, but did not provide a detailed explanation of how the data was collected. From the data, Wetzel observed that the distribution of maximum stalk height occasionally resembled a Rayleigh distribution, but the distribution could vary significantly for different rain conditions with the same rate. Therefore,

the relationship between stalk height distribution and rainfall conditions remains unclear.

Rain-induced surface waves, also known as ring waves in the case of single drop impacts, have been studied in laboratory settings. Houk and Green [26] utilized a capacitance wave gauge to measure the surface waves generated by artificial rain. Their raindrop distribution consisted of drops with diameters near 2.2 mm (73%), 3.6 mm (23%), and 5.5 mm (4%), with all drops impacting a thoroughly mixed receiving water at speeds within 1% of their terminal velocity. Houk and Green [26] discovered that the root mean square (RMS) surface height fluctuation was directly proportional to the kinetic energy flux of the rain, raindrop size, and inversely proportional to the liquid viscosity. Bliven, Sobieski, and Craeye [27] conducted an experiment with 2.8 mm diameter raindrops impacting a target pool at terminal velocity, with an artificial rain rate ranging from 5 to 200 mm per hour. They concluded that the energy of rain-induced surface waves is primarily found within the range of 2 to 15 cm wavelength, with the maximum wave energy occurring at a wavelength of approximately 5.3 cm.

Study on secondary droplets generated by an artificial rain field impacting a deep water water pool remains untouched.

Chapter 2: Experimental Details

The droplet experiment was conducted in the Hydrodynamics Laboratory at the University of Maryland. The facility, depicted in Figure 2.1, comprises a target pool (representing the ocean) and a rain generator positioned approximately 2.2 meters above the pool. We also installed a water filtration system, a cooling system, and a rain reservoir to generate raindrops with specified temperatures. To measure the secondary droplets, we employed a cinematic in-line holography technique, which generates time-resolved images for later analysis using MATLAB.

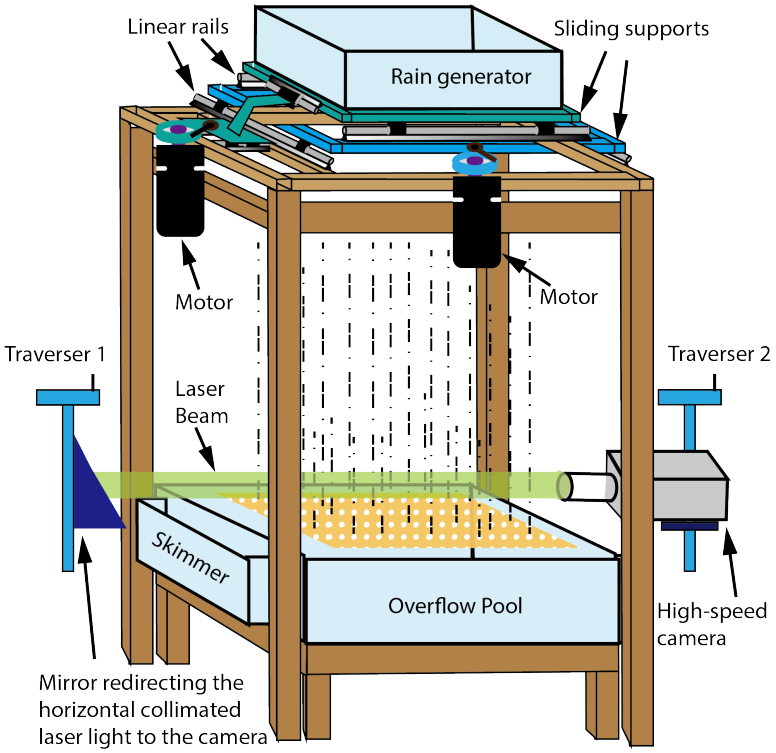

Figure 2.1: Rain Facility

2.1 Experiment Facility

2.1.1 Target Pool

The target pool, is a square tank constructed of transparent acrylic material, measuring 1.2 meters by 1.2 meters and with a depth of 0.31 meters, as illustrated in Figure 2.1. The tank is elevated approximately 0.5 meters above the ground by four short legs, which are adjusted to ensure the tank is level. To maintain a constant "sea level," the tank features two overflow pools situated 1.27 centimeters above the tank's edges. The overflow pools can ensure a constant water surface level when the artificial rain is falling.

2.1.2 Rain Generator

A rectangular shaped open surface water tank is installed at the top of the frame. There is a rectangular array of 369 equally spaced hypodermic needles at the bottom surface of the tank to make constant raindrops. The needles used are 22-gauge with an inner diameter of 0.41mm, and the length of the needles is 6.4 mm. The orientation of the needles is the half field concentrated orientation from Ren's setup [30]. As shown in Figure 2.2b, the 369 needles are placed in 9 odd rows and 9 even rows, and the distance between the needles is uniform, 2.54 cm. The red area on the figure is sealed using waterproof silicone sealant and remains unused in this experiment.

In order to maintain a constant rain drop size (1.41 - 1.54 mm in radius) and rain rate, the depth of the water in the rain tank is maintained at about 10 cm by using a drainage tube connecting to an overflow tube.

The tank is mounted on a linear traverser system that can move linearly in two directions.

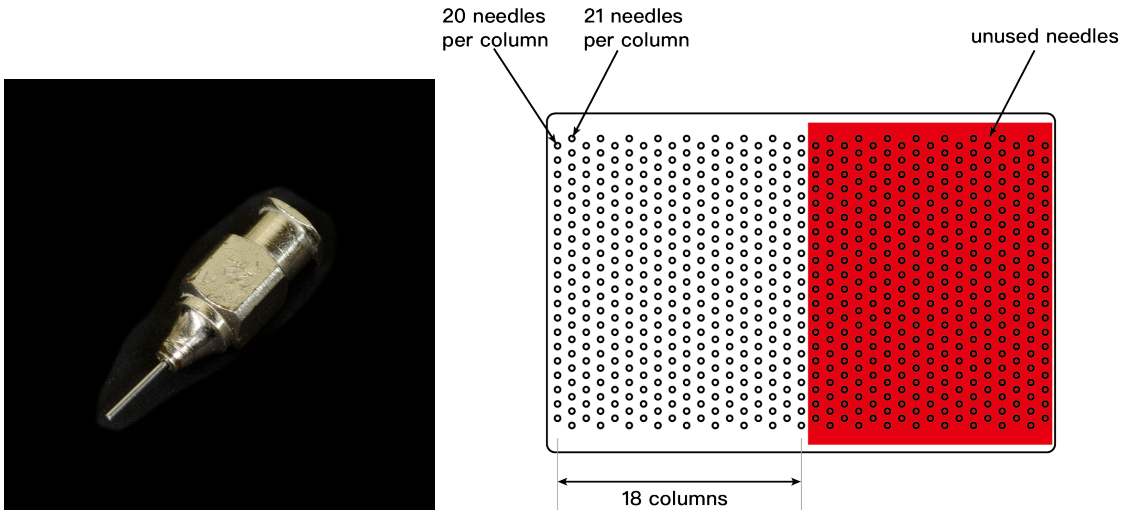

(a) Needle (b) Needle Orientation

Figure 2.2: Rain Generator

The traverser is controlled by two linear motors with feedback control software, and for this experiment we try to make the rain tank move in a circular motion to prevent raindrops fall onto the same spot. The diameter of the circular motion is about 2.5 cm and the frequency of the motion is 0.5 Hz.

2.1.3 Water Preparation

Previous studies showed that the surface tension is an important factor in liquid to liquid impact, so clean fresh water is needed before every experiment using a special procedure. There are three levels of filtration system for the water used in this experiment. The first level is a 20 μm filter to remove anything that's larger than 20 μm. The second level is a 5 μm filter that's added on the water pump for circulating the water. The third level filter is also a 5 μm filter which has been added on the cooler unit, and it only provides additional filtration when the cooler is in use.

In the morning, the ocean tank and the rain reservoir are cleaned using water with high

concentration pool chlorine to clean out all the possible microorganisms. Then the ocean and the water reservoir is filled with filtered water, and pool chlorine is added to the water such that the water has a free chlorine of 5 ppm. The chlorine level is tested using a pool tester. Then the water is circulated for a day using the filtration system with the 5 μm filter. On the second day, the water is circulated for another 2 hours in the morning before everything else starts.

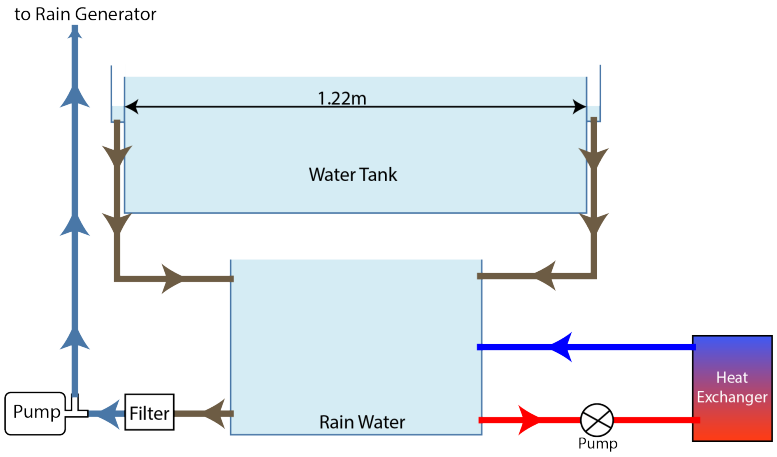

Figure 2.3: Circulation, Filtration and Temperature Control

2.1.4 Temperature Variation

A separate cooling system is added to cool the rain water, a heat exchanger is used to control the temperature of the rain. The chiller is connected to the rain reservoir, and there are 2 thermal couples were placed inside the rain tank and the ocean to ensure the rain temperature is at the required range, while keeping the ocean temperature constant.

There are three designed temperature conditions for the experiment. To achieve desired temperature, the water in the rain reservoir is cooled by the heat exchanger to the desired temperature. A thermometer is built in the heat exchanger to examine the temperature of the water. Due to the limitation of the heat exchanger, the lowest rain temperature was approximately 8 degree Celsius.

At this temperature, water is 0.25% less dense than the highest water density (around 4 °C).

2.1.5 Temperature Measurement

Two T type thermal couples are used to measure the transient temperature during the experiment to make make sure the variation is not far from the desired values. One thermal couple is placed inside the rain tank to measure the temperature of the rain, the other one is placed about 10 cm below the ocean surface to record the temperature change of the ocean water body. A USB thermocouple data acquisition module from Omega was used to take the temperature measurement.

Actual temperature measurements are shown in Figure 2.4 including rain temperature and temperature of the target pool. Every marker in the plot is an average temperature through a single run, and the dashed line is an average temperature over three runs. It is shown that the temperature variation between runs are fairly small comparing to the change in different temperature conditions. Also the temperature of the target pool has been kept somewhat constant throughout the whole experiment.

2.1.6 Surface Tension Variation

Triton x-100 was added into the ocean to simulate ocean surface with different surface tension. It is important that we only add surfactant in the ocean while keeping the rain clean because that's what happens in the ocean. Three surfactant levels are added into the tank: 5ml, 15ml, and 60ml, and three resulting surface tension values are recorded. The highest surfactant level results to a critical micelle concentration, and at this concentration, the surface tension

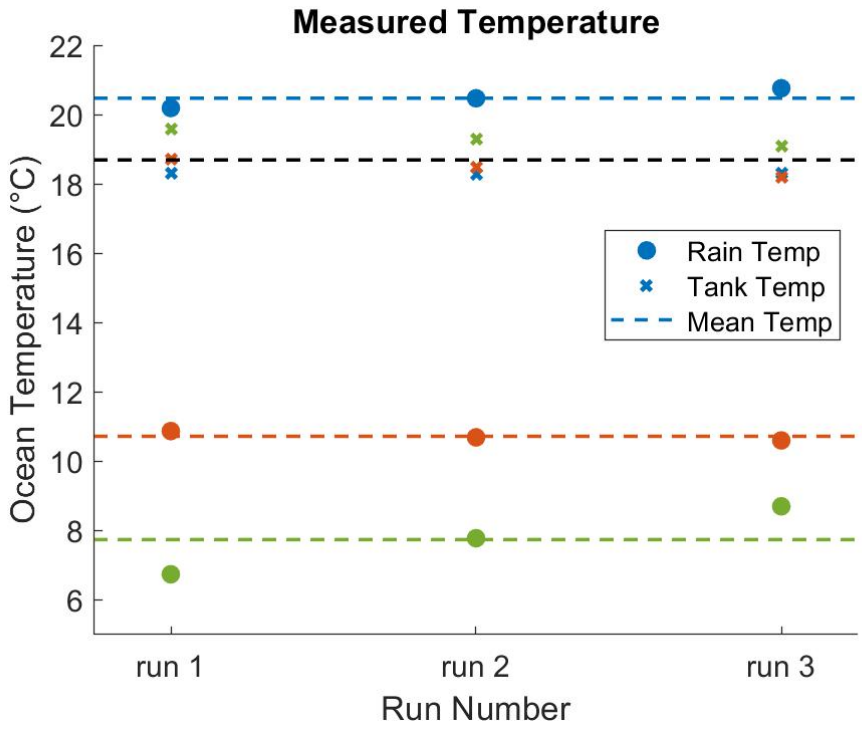

Figure 2.4: Temperature Measurement During the Experiment

reaches the lowest value (about 35 mN/m).

2.1.7 Surface Tension Measurement

The process to take isotherm surface tension measurement is reported by Martin Erinin in 2020. I will restate the process here for the purpose of completeness. The surface tension isotherm was measured using a Langmuir trough from KSV Nima at the beginning and the end of each experiment day. The equipment consists one Teflon trough and two barriers were completely cleaned using tap water. When taking measurements, a water sample is collected from the middle of the ocean with a 500 mL beaker, which is used to rinse the trough and the barriers. Another 500 mL is then collected and added into the trough. The surface tension is measured by an electronic balance connected to a platinum Wilhelmy plate which is in contact with the water surface. The

surface tension creates a downward pull on the plate and then transferred to the balance to create a reading which can be recorded using their software. The isotherm curve is measured when the two barriers compress the water surface area, causing the surfactant on the water surface to be compressed into a smaller area, resulting a decrease in the surface tension measurement.

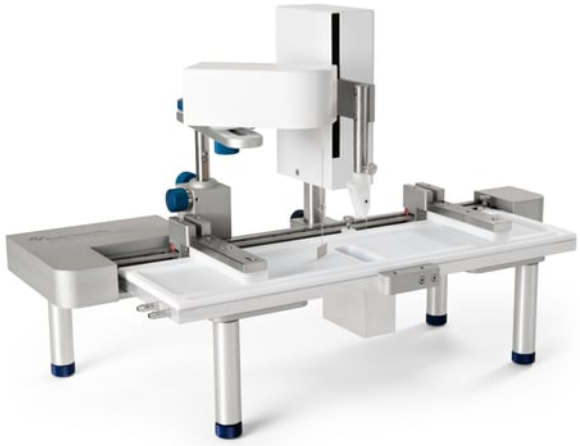

Figure 2.5: KSV NIMA Langmuir Trough Used for Surface Tension Measurement [31]

Case 1 in Figure 2.6 shows an isotherm curve for clean water (water without adding surfactant and properly circulated), and case 2-4 shows three pairs of the isotherm curve taken before and after the surfactant runs. Ideally, without any surfactant, the isotherm curve should be a horizontal line with a value of about 74 mN/m, however, in reality, it is said that the water is clean enough if 1) the value of the surface tension is about 74 mN/m, and 2) the surface tension does not drop significantly after about 70% of compression, and with which said, case 1 is considered clean. We could also see that the slopes of case 2 and 3 is very steep because of the compression of the surfactant.

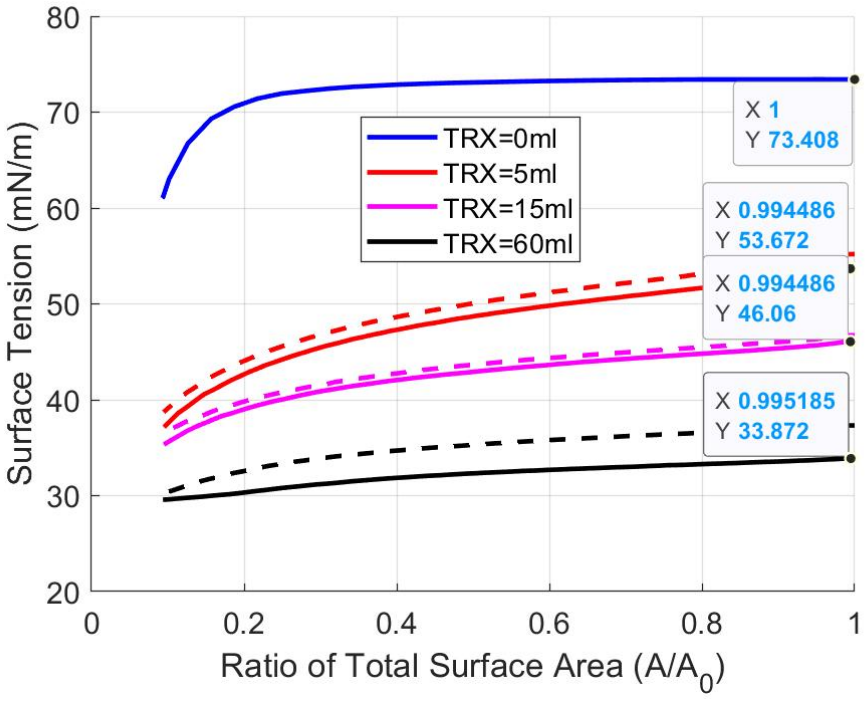

Figure 2.6: Surface Tension Measurement During the Experiment: From top to bottom are case 1 to 4.

2.2 In-Line Holography Technique

Holography is a three dimensional (3D) imaging technique that can resolve 3D position information by capturing the interference patterns formed by the collimated laser beam itself and the diffracted light at the edge of the object. Figure 2.7 is a sample image of one single droplet, and it appears to be a circular interference pattern which is formed by the collimated beam and the diffracted light by the edge of the object. Thanks to the recent development in both digital cameras and the computing power, holography has been used in many areas to measure the 3D position and the size of the particles that has circular shapes Katz and Sheng [29]. A form of holography where the reference laser beam is coincident with the camera axis is called in-line holography which is used in the present experiment due to its simplicity in setup and post

processing.

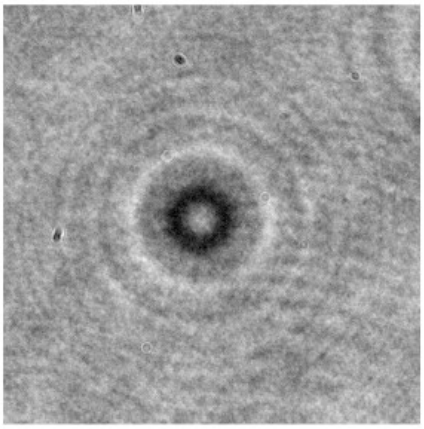

Figure 2.7: Holographic Image of a Single Droplet

In line holography uses a coherent and collimated laser beam as the illuminating light source. The camera's line of sight is coincident with the axis of the laser beam. As shown on the Figure 2.9, the testing volume is the cylinder that the collimated beam passes through. Hologram is the images that are recorded by the camera sensor when an object (droplets in this case) passes through the testing volume. The interference pattern contains the phase and amplitude of the diffracted waves [29]. This information is the key to perform 3-D reconstruction using image processing techniques. The physical setup includes a coherent and collimated laser beam as the light source and a high speed camera that is used to record high frequency data. The following parts will discuss them in detail.

2.2.1 Laser Setup

The collimated beam used in in-line holography measurement is delivered by a low power Nd:YLF laser (CrystaLaser QL527-100), and even though it's a low power laser, we still need to add neutral density(ND) filters to further decrease its intensity to prevent over exposure. The beam passes through two ND filters to decrease its intensity to about 50%, then goes through a spatial filter to increase its quality. The more uniform light beam is then collimated by passing through an achromatic concave lens and an achromatic convex lens to expand and then converge the light beam. The collimated beam is then directed horizontally across the ocean at three different heights above the water surface: 4.45 cm, 6.99 cm, and 9.53 cm (in accordance to 1.75 in, 2.75 in, and 3.75 in).

Newport 900 three axis spatial filter is used for the laser setup, along with a M-10X objective lens and a pinhole with 10 μm diameter. The combination of the pinhole diameter and the objective lens focal length can be calculated by the equation:

$$D_{opt} = \frac{F_{obj}\lambda}{r_{beam}} \tag{2.1}$$

where D_{opt} is the optimal pinhole size, F_{obj} is the objective lens focal length, and r_{beam} is the input beam radius. An objective lens with 10X magnification and 16.5mm focal length (Newport Optics, model M-10X) was chosen, the wavelength of the laser is 527 nm, and the input beam radius is approximately 0.77 mm. Using Equation 2.1, the optimal pinhole diameter is found to be approximately 10 μm.

The collimation of the beam is performed by using a set of lenses including an achromatic

concave lens and a convex lens. A shear-plate collimation tester mirror that has a small angle between the two surfaces is used to test if the beam is parallel. The tester mirror is placed in a 45 degree angle with the light beam. If the light beam is collimated, the reflected light will have parallel fringes that are wide and horizontally oriented. As shown on Figure 2.8, as we change the distance between the concave and convex lenses, the beam becomes more and more collimated until it reaches the perfectly collimated image.

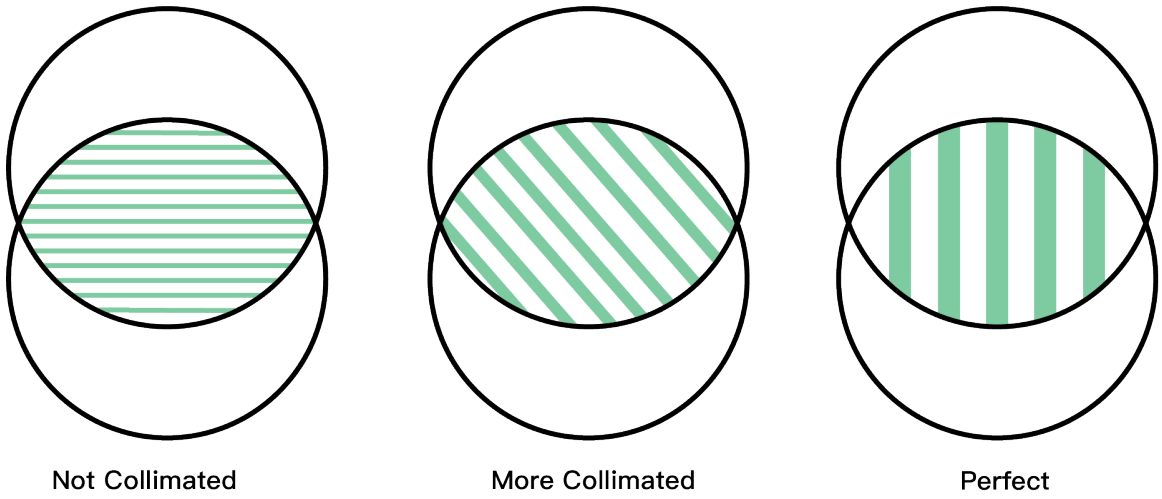

Figure 2.8: Beam Collimation Tester

2.2.2 Camera Setup

A high-speed digital cinematic camera (Phantom) equipped with a long distance microscope lens (Infinity K2) was placed on the opposite side of the ocean from the light source. The camera and the lens is aligned such that the optical axis of the lens is coincident with the collimated laser beam, and the face of the sensor is perpendicular to the axis. The alignment process is needed at every one of the three different heights, and the center of the images are at the heights stated above. The laser pulse and the camera are synchronized using a delay box to take holographic

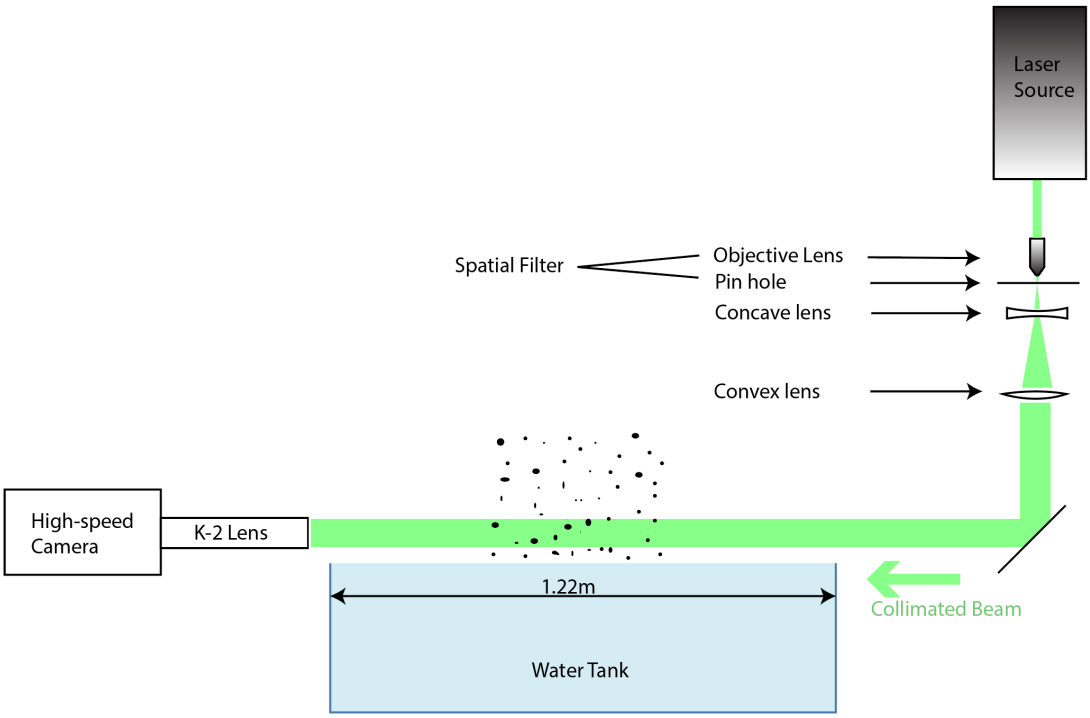

Figure 2.9: Camera and Laser Setup

image at a rate of 1000 Hz.

2.2.3 In-Line Holography Calibration

The in-line holographic system is calibrated with a custom calibration target, as known as ”the reticle”. The reticle is a circular glass with 14 sputter deposited circles with diameters varied from 30 μm to 3000 μm, as shown on Figure 2.10. There is in fact no ”calibration” process needed, the following calibration process was performed for two purposes: 1) ensure the magnification of the lens is approximately 1:1, 2) ensure the smallest droplets (d = 100 μm) can be caught on the furthest end of the ocean, and 3) quantify the reconstruction error for the drop diameters.

To achieve the target 1), first, the reticle was placed near the focal plane of the lens (near the

(a) (b)

Figure 2.10: White Light Images of the Reticle

middle of the ocean), then the focus was adjusted accordingly to make the image sharp. Figure 2.11 shows a sample holographic image when the reticle is at the focal plane. The image size of the 1000 μm-diameter circle is about 100 pixel, which means the magnification is about 1:1.

To achieve 2) and 3), the reticle was installed on a manual traverser, and the reticle was traversed through the whole testing volume, and data was taken at every 10 cm. Figure 2.12 shows the original image and the reconstructed image at the farthest end of the ocean, and it is clear that the drops with 100 μm diameter appears to be sharp and in focus in the image. Also, with this data, the error in the reconstructed diameter was assessed to be no more than 3% over the entire width of the ocean.

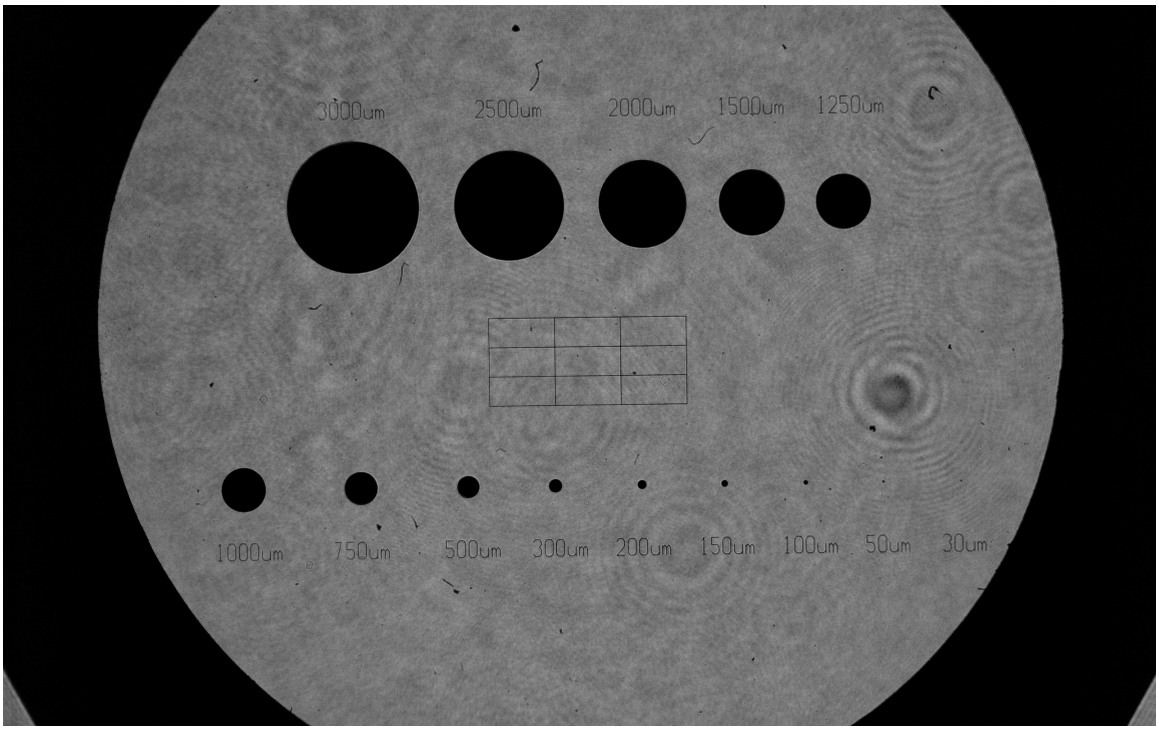

Figure 2.11: Example Holographic Image of the Reticle (In-Focus)

2.3 Data Processing Technique

There are three parts in the data processing. First, the raw images are reconstructed through a hologram processing algorithm which extracts the size and the 3-D location of the droplets from the original image. The reconstructed data goes through a droplet tracking code to connect the drops into individual tracks. Finally, the connected data structure is revisited by a data cleaning and connecting algorithm to take out unwanted tracks. During the process of reconstruction, cluster from a High Performance Computer (HPC) called Zaratan from University of Maryland is used to accelerate the process.

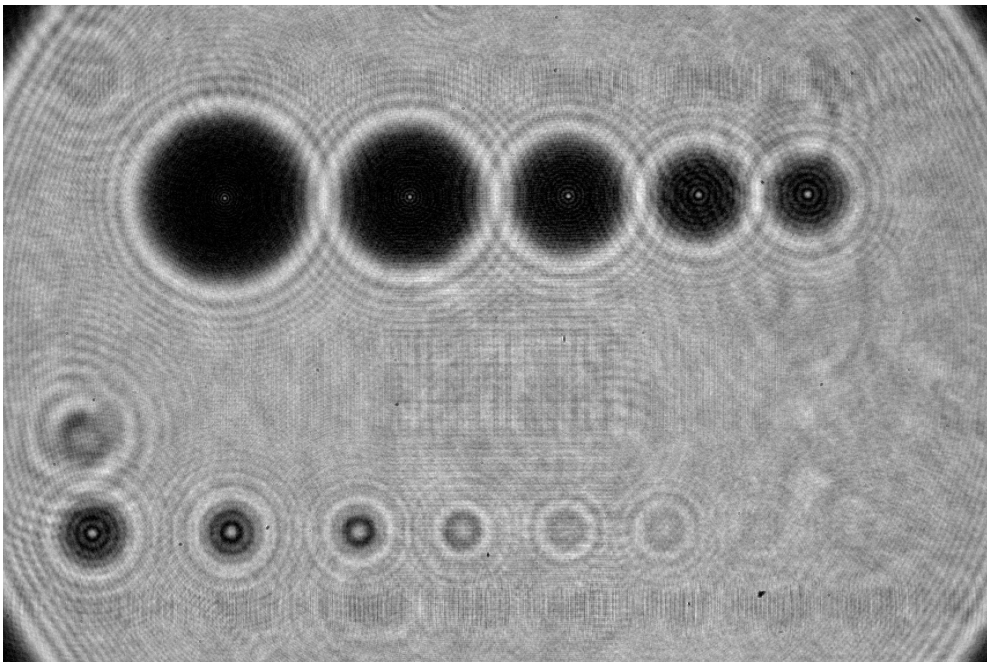

(a) Original

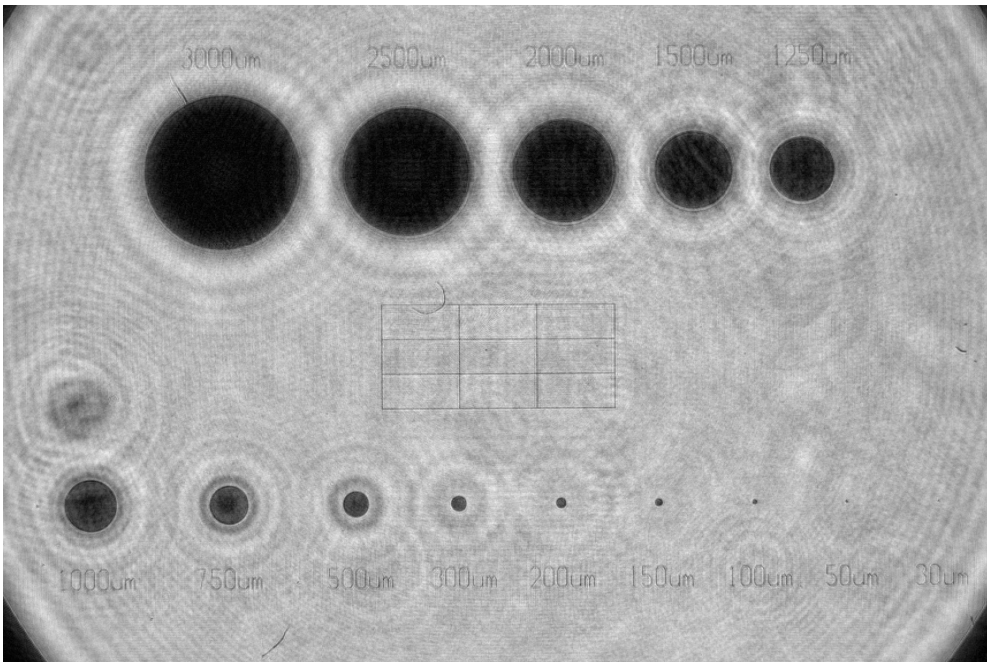

(b) Reconstructed Image

Figure 2.12: Images of the Reticle at Farthest End of the Tank

2.3.1 In-Line Holography Reconstruction

After in-line holography data was taken from an experiment, the images can be digitally reconstructed at any position in the depth direction (z direction, along the collimated laser beam) by using a model developed by Katz and Sheng [29]. The basic principal of reconstructing the images is to find the z location where the edge of the drop appears to be the sharpest. Figure 2.13 shows an original image along with reconstructed images around the actual z location of the droplet. When the actual location of the droplet is found, the circle appears to be dark in the middle and has a sharp edge. When the image is reconstructed away from the droplet plane, it appears to be out of again with interference patterns.

Figure 2.13 also shows images of a droplet that was at 189 mm away from the focal plane of the K2 lens ($z_0 = 189\ mm$). The bottom series of images show the reconstructed holograms around $z = 189\ mm$, and it appears to be coming in focus and goes away from the focus (as reconstruction distance z goes near and away from 189 mm). The drop that's marked as $z = z_0$ appears to be fairly sharp and dark in the middle, so we say $z_0 = 189\ mm$ is the actual z location of the droplet, and the size of the circle is the actual size of the droplet.

The GPU compatable reconstruction algorithm that was provided to us and developed by Professor Joseph Katz form Johns Hopkins University was modified and used in this experiment. We just want to acknowledge Professor Katz and his research group for the generous of sharing the algorithm with us.

The drop-finding MATLAB algorithm determines the z location of the droplets, then finds the x and y coordinates and the diameter of the drops. This algorithm is developed in-house and it is loosely based on the Hybrid method proposed by Guildenbecher et al. [28]. The process was

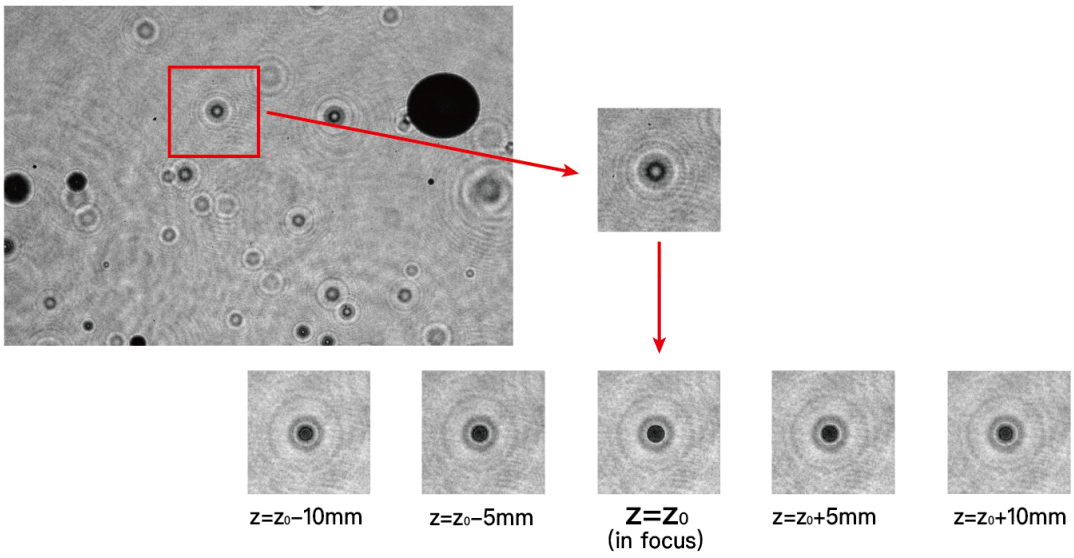

Figure 2.13: Example Image of the Reconstruction Process

originally discussed in the PhD dissertation from Doctor Martin Erinin, here I will restate it for the purpose of completeness. The steps taken are as following (modified):

1. Reconstruct the image every 1000 μm along the testing depth (half of the ocean width), resulting in a reconstructed image series.

2. Detect the droplets by thresholding, record the radius and x, y location information of the droplets detected.

3. Calculate a mean sharpness criteria at each reconstruction step.

4. Find the plane where the image is the sharpest, record z location and refine the recorded radius above.

5. Save reconstructed data into a MATLAB data structure including center, diameter, z distance, and the sharpness criteria value for the next steps.

There are some steps that are modified from the original version of the algorithm. First, the pre-process of the image is not needed since there is not a significant background noise in the data taken in this experiment. Then, there were two reconstruction steps including a rough one and a more close one. In this version of the algorithm, the two steps are merged into one step with a smaller reconstruction step. Finally, the reconstruction progress is parallelized using MATLAB's parallel computing toolbox to increase the processing speed.

2.3.2 Reconstruction Accuracy Validation

To understand the accuracy of the algorithm, a reticle target is placed on a traverser, and data is taken at every 100 mm throughout the total measurement field. Then, the holographic images of the reticle is processed using the same algorithm that reconstructs the actual data. The reconstructed radii versus actual radii is plotted on a plot to see the linear relationship. The magnification of the k-2 lens changes with different focus location, so to test if the magnification changes the accuracy of the reconstruction, a validation with about 1.35x magnification was also performed and plotted. The detected radii of the reticle target has a mean absolute error of 0.0573 mm.

2.3.3 Parallel Computing and High Performance Computer

The new High Performance Cluster (HPC) called Zaratan at University of Maryland is built and offered to all researchers for free in 2022. Thanks to Professor Xinan Liu's help, we were able to further modify the drop-finding algorithm to adapt to the High Performance computing cluster at University of Maryland using parallel computing toolbox in MATLAB.

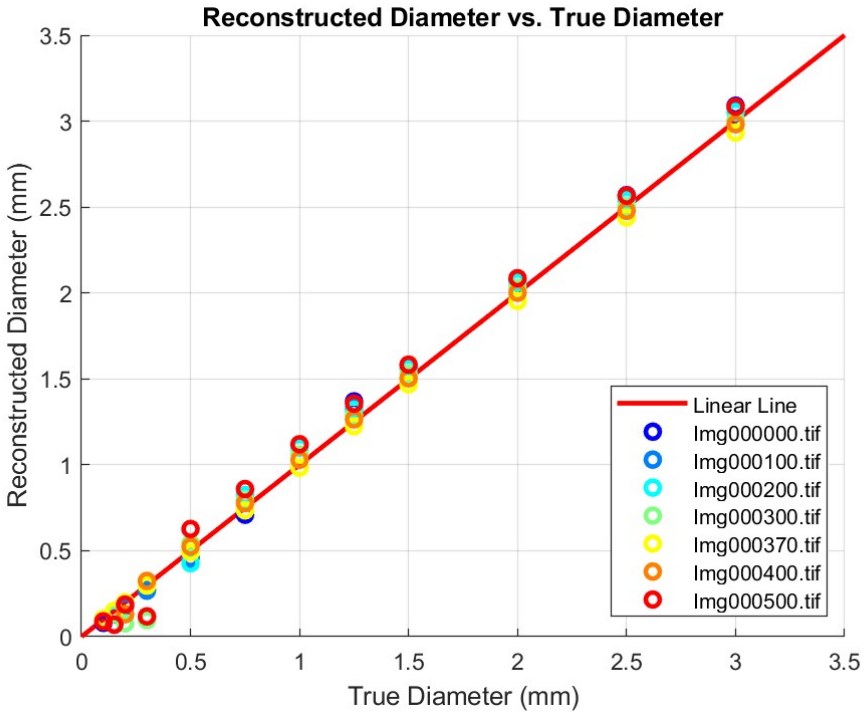

(a) Magnification = 1x

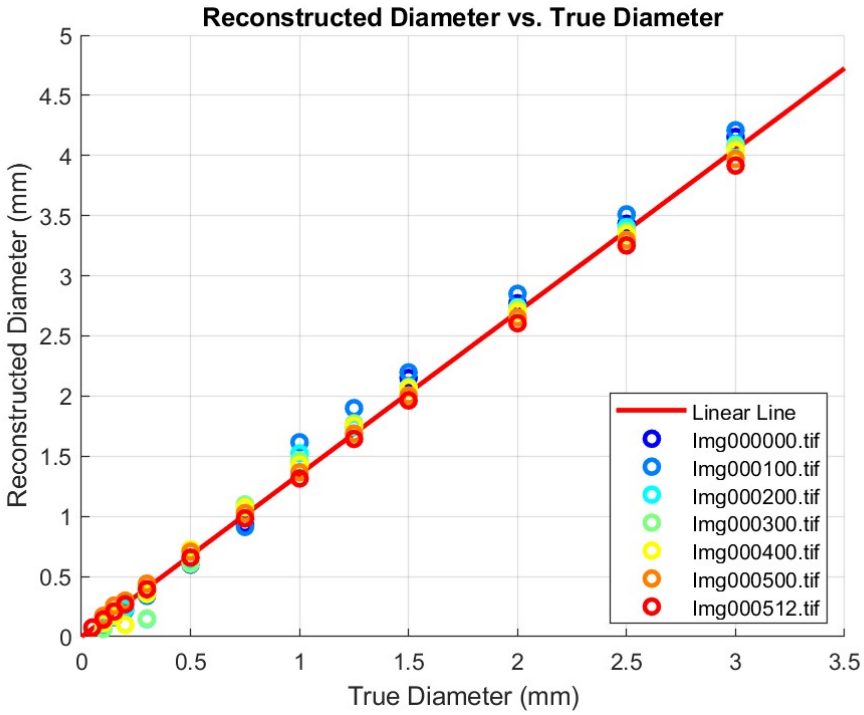

(b) Magnification = 1.35x

Figure 2.14: Validation of Accuracy of Reconstruction Algorithm

Parallel computing is a technique that could allow multiple computing sessions going on at the same time to decrease the computational time required for the job. Any process that does not require sequential output and is independent from each other could use parallel computing to increase the performance. In our case, the reconstruction of the image series.

So we decided to parallelize the process of the reconstruction of the images. MATLAB *parfor* command was used to make the process parallel. While the parallel in progress, GPU is also used to increase the speed of the calculation. It is stated by MATLAB documentation that a single GPU device can only be used by one worker at a time, meaning the number of workers should be the same as the number of GPU devices. However, in practice, the performance increases as we increase the number of workers, as the test trails suggests, 2 to 3 workers per GPU device.

The challenge in adapting the program to the cluster is that the program uses both CPU and GPU. Many test trials were performed to ensure the resources required is efficiently used. There are 4 parameters that we need to specify for this type of job: 1) number of nodes, 2) number of workers, 3) memory required per worker, and 4) number of GPU. After 20 test trails, the optimized configuration is 15 workers on a single node, with 4 NVIDIA A100 GPUs per node and 8GB memory per worker. With such configuration, the reconstruction and droplet detection process is 4 times faster than using the local workstation.

2.3.4 Droplet Tracking

After reconstructing the holography images and locating the drop, an in-house MATLAB particle tracking code was developed based on existing algorithms to adapt to this experiment.

There are some challenges in the present experiment that we need to solve. First, the velocity variation of the droplets is large comparing to traditional particle tracking application. For example, one drop can reach its highest position within the frame, and stay in the movie for 20 frames. In comparison, another fast-moving droplet might only be in the view for 5 frames. This variation in velocity make it hard for the traditional nearest neighbour tracking algorithm to work appropriately.

Another challenge is that due to the large size and high intensity of the droplets, the drops might block each other and collapse to one large spot on the image for several frames, in some extreme cases, more than 5 frames. This especially challenges algorithm because it is difficult for the algorithm to resume tracking the trajectories after the obstruction.

Chapter 3: Results and Discussion

3.1 Overview

In this chapter, we present and discuss the experimental results pertaining to the formation of secondary droplets resulting from a rain field entering a deep water pool. The experiment was conducted under various conditions, particularly focusing on temperature variations. As a result, the characteristics of the rain field, including raindrop size, rain intensity, and impact velocity, were found to differ across the different cases. Each section provides a detailed analysis of these characteristics specific to the respective experimental conditions.

Furthermore, we specifically focus on the secondary droplets with a radius exceeding 50 μm, examining three different rain temperatures (T_{Rain}) and four different levels of water pool surface tension (ST). Remarkably, we observed a significant impact, up to 50%, on both the rain temperature and surface tension, albeit influencing different parameters. These findings will be thoroughly explored within this chapter.

It is worth noting that due to challenges in recognizing and tracking secondary droplets when their concentration is high, all the results presented were obtained when the camera was positioned 3.75 inches above the water surface. Thus, all the discussions in this section specifically pertain to the region 3.75 inches above the water surface. Nonetheless, we have collected raw data at lower heights, which can be processed once a more capable algorithm is developed.

This chapter consists of two sections, each focusing on a different experimental condition: rain temperature and target pool surface tension. Within each section, we delve into the characteristics of the generated rain field, analyze the total number of secondary droplets, and discuss the droplet production in detail. The term ”total secondary droplets” encompasses all the droplets captured and tracked during the experimental duration, regardless of their movement. Additionally, we consider any tracked trajectory with an upward velocity as an indicator of secondary droplet generation. This dataset allows us to estimate the quantity and behavior of the generated secondary droplets. Notably, this generation data includes all the secondary droplets detected by the camera sensor, regardless of their localized generation.

3.1.1 Experiment Conditions

There are in total six different experimental conditions that are listed below. Some details about rain field is listed as well. The room temperature case and the clean water case are the same trials since all the designed conditions are the same. As presented in the table, the droplet diameters are nearly the same for all trails; the average radius for all the cases is $\overline{R}$ = 1.46 mm and the standard deviation is $\pm$ 0.05 mm. However, upon calculating, the rain rate could be affected by the rain temperature by about 25 %. The impact Weber number and Froude number is calculated by using equations:

$$We = \frac{\rho V^2 D}{ST} \tag{3.1}$$

$$Fr = \frac{V^2}{gD} \tag{3.2}$$

where ρ is the liquid density, V is the average impact velocity, D is the average rain drop diameter, and ST is the surface tension. The data used in this equation is averaged over runs and individual rain drops. It is shown that the experiment Weber varies from 1201 to 2441, and the Froude number does not change much because both the rain diameter and the impact velocity does not vary in our cases.

Table 3.1: Experimental Conditions Listed

Case Name	$\overline{T}$ (°C)	ST (mN/m)	$\overline{R}$ (mm)	Rain Rate (mm/hr)	ν (10^{-6} m^2/s)	Re	We	Fr
T 1	7	73.4	1.54	218.0	1.430	12100	1307	1.018
T 2	10.8	73.4	1.53	254.6	1.278	13316	1283	1.018
T 3	20.2	73.4	1.44	295.2	0.997	15976	1201	1.044
S 1	20.2	35.6	1.43	248.0	0.997	15810	2441	1.044
S 2	20.2	46.5	1.41	248.2	0.997	15634	1850	1.052
S 3	20.2	54.4	1.41	268.8	0.997	15590	1573	1.048
S 4	20.2	73.4	1.44	295.2	0.997	15976	1201	1.044

Case TEMP 3 and TRX4 are the same case with rain drops at rain temperature and clean target pool water.

3.2 Rain Temperature Effect

3.2.1 Effect on Generated Rain Field

Upon examining the temporal data of raindrops across different runs with the same experimental conditions, it was observed that the resulting rain field remained constant over time. Therefore, we were able to average the data obtained from all the runs. The average standard deviation in raindrop radius for the temperature case was found to be 0.1383 μm.

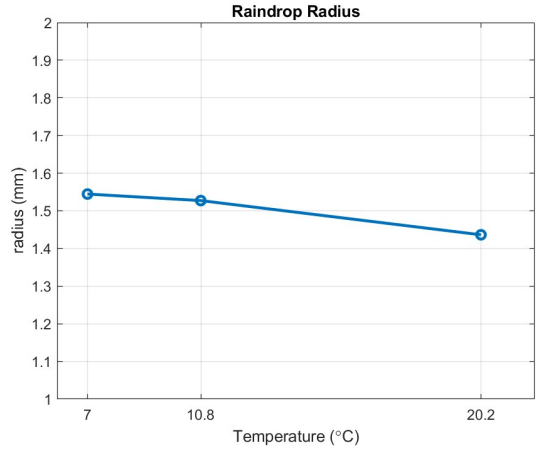

(a) Radius

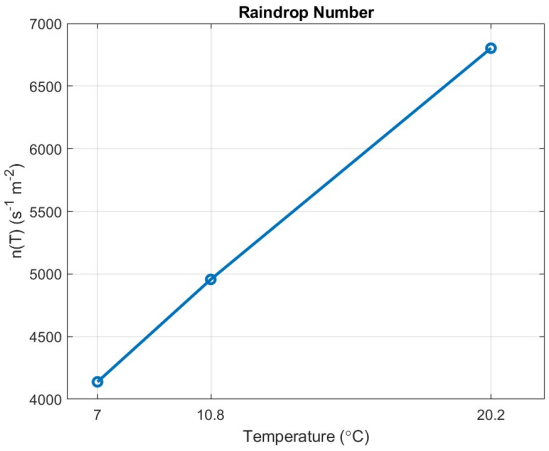

(b) Raindrop Number

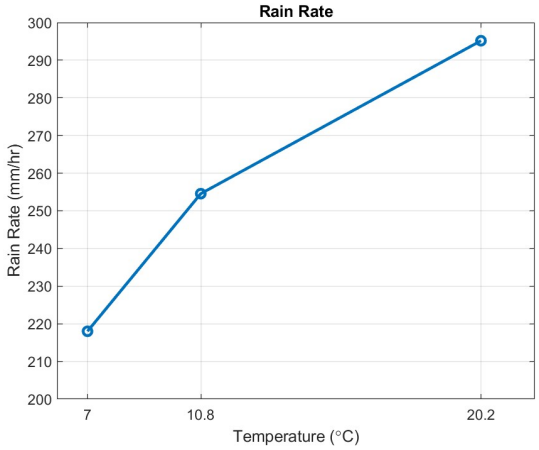

(c) Rain Rate

Figure 3.1: Rain Field Specifications Versus Rain Temperature

The total number of raindrops presented here represents the average number of raindrops over three runs throughout the entire movie duration of 12.47 seconds. Figure 3.1 illustrates the changes in average radius, raindrop number, and rain rate with varying rain temperature. It can be observed that as the rain temperature approaches room temperature, the size of the raindrops decreases by approximately 7%, while the total number of droplets increases by 65%, resulting in a 40% change in the rain rate (Figure 3.1c). The velocity of the raindrops does not exhibit significant changes, with an average impact velocity of $\overline{V}_{rain} = 5.58m/s$, with a standard deviation of $SD = 0.02m/s$.

3.2.2 Secondary Droplet

3.2.2.1 Droplet Number

To calculate the droplet number, we divided the total number of droplets by the total number of raindrops. This approach was necessary since the number of raindrops varied among the different cases. Figure 3.1b demonstrates the significant changes in raindrop number as the rain temperature varies. However, in the subsequent section concerning target pool surface tension, the raindrop number shows relatively minimal variation compared to the temperature case.

As depicted in Figure 3.2, decreasing the rain temperature leads to a dramatic increase in the number of secondary droplets per raindrop. The count rises from approximately 31 to 47 drops per raindrop, resulting in a change of over 50% in quantity. This phenomenon could be attributed to the larger raindrop size observed in cases with lower temperatures compared to room temperature. Another potential factor is the increased viscosity of water at lower temperatures (Table 3.1). The production of secondary droplets follows the same trend, exhibiting an increase

of over 50%. This may be influenced by the change in viscosity. As the temperature gets lower, an increase in raindrop viscosity is observed. We suspect that this increase in raindrop viscosity has promoted the generation of secondary droplets.

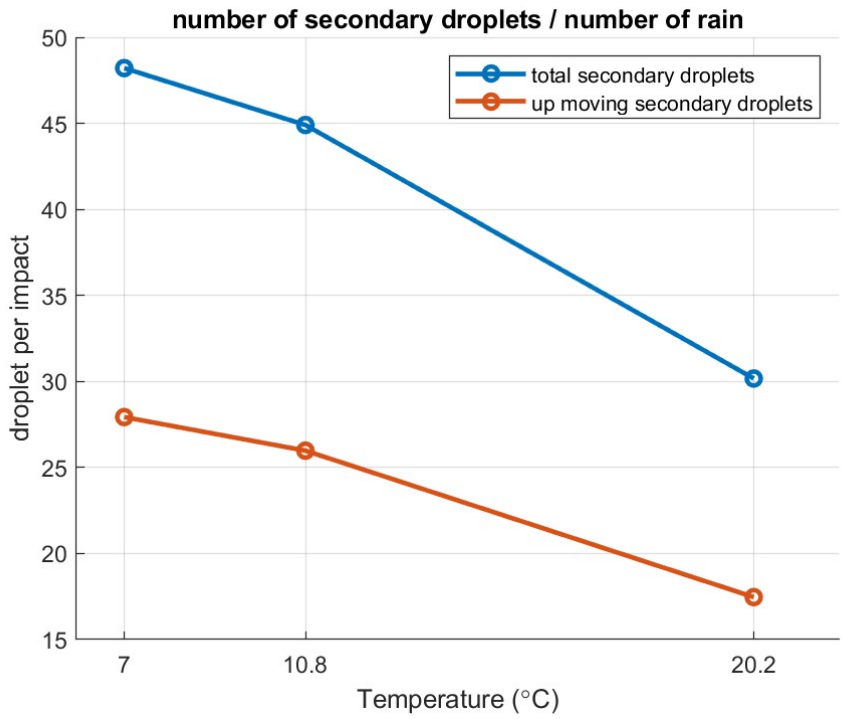

Figure 3.2: Secondary Droplet Number

3.2.2.2 Droplet Size

Figure 3.3 presents the average droplet size as a function of rain temperature. The average droplet radius was calculated based on data obtained from three runs conducted for each case. The results indicate that changing the rain temperature has a minimal effect on the average size of secondary droplets.

The average size of the total droplets is smaller than the average size of the produced droplets. This observation can be attributed to the behavior of droplets during the experiment.

Smaller drops have a higher likelihood of reaching higher positions and therefore traveling longer in space. The portion of the total droplets which are smaller in size and generated in the area that is not directly below the testing volume makes the average size of the secondary droplets smaller.

The mean droplet radius exhibits a change of less than 5%, indicating that there is no significant alteration in the mean droplet size when the rain temperature is varied. The Sauter mean of the droplet radius is a ratio of the volume and surface area, and this quantity has a fairly large change with varying temperatures.

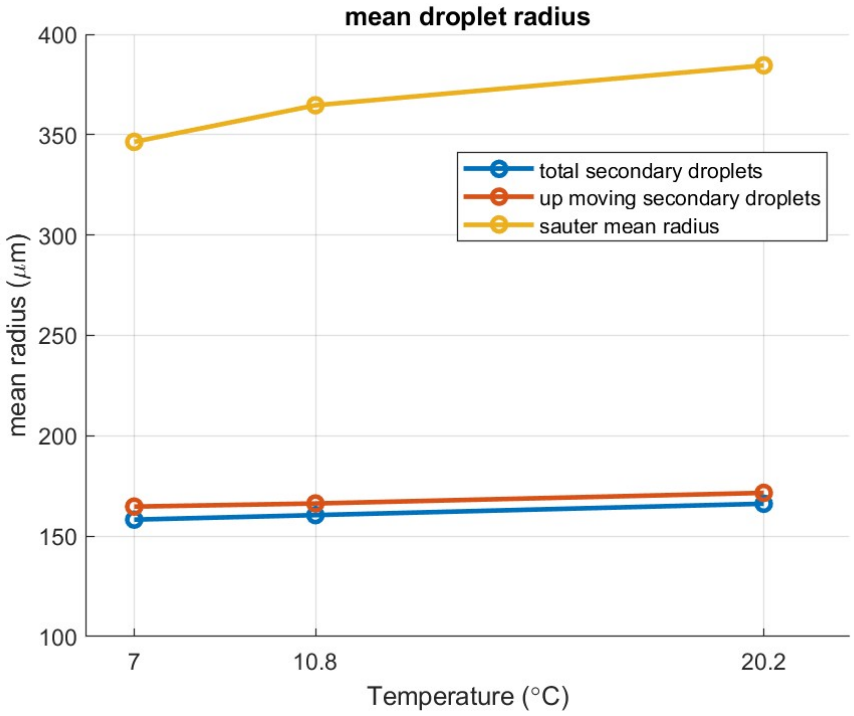

Figure 3.3: Secondary Droplet Size

Figure 3.4 shows distributions of the radii of the secondary droplets with different scales to see different behaviors. Figure 3.4a shows a layered bar plot of the secondary droplet radius. For different temperature cases, it is shown that as the temperature decreases, an increase in smaller droplets appeared (R = 80 μm) on the left side of the figure. This change in distribution can also

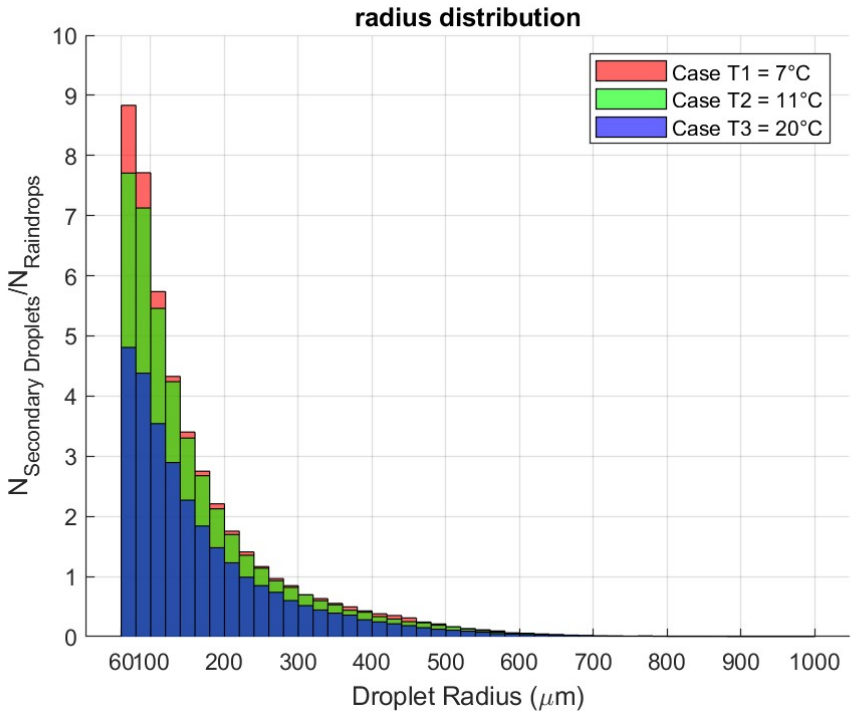

(a) Barplot

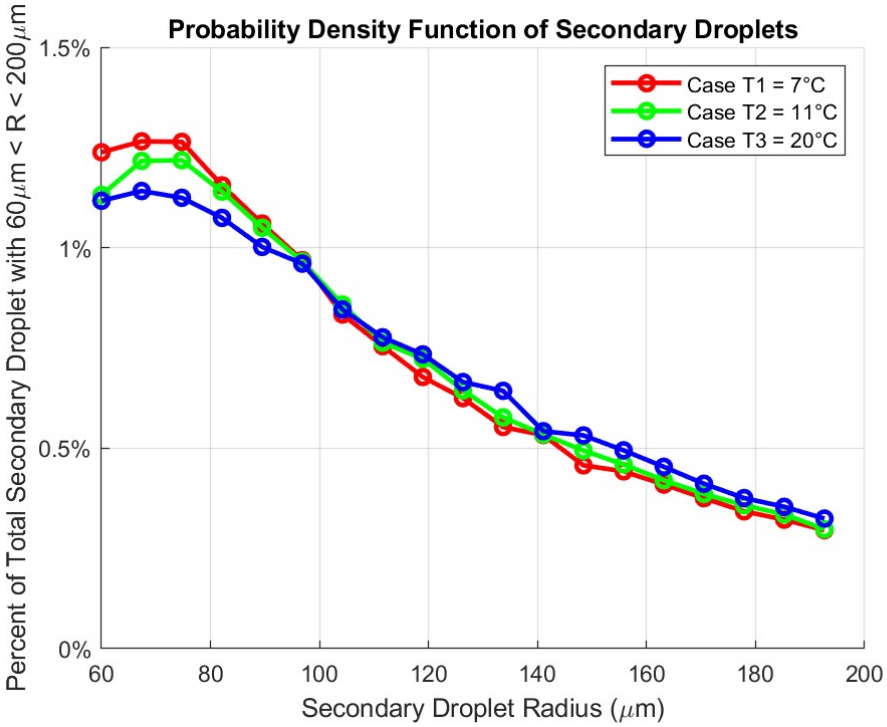

(b) Linear-Linear Plot for $60 < R < 200\mu m$

Figure 3.4: Radius Distribution of Secondary Droplets

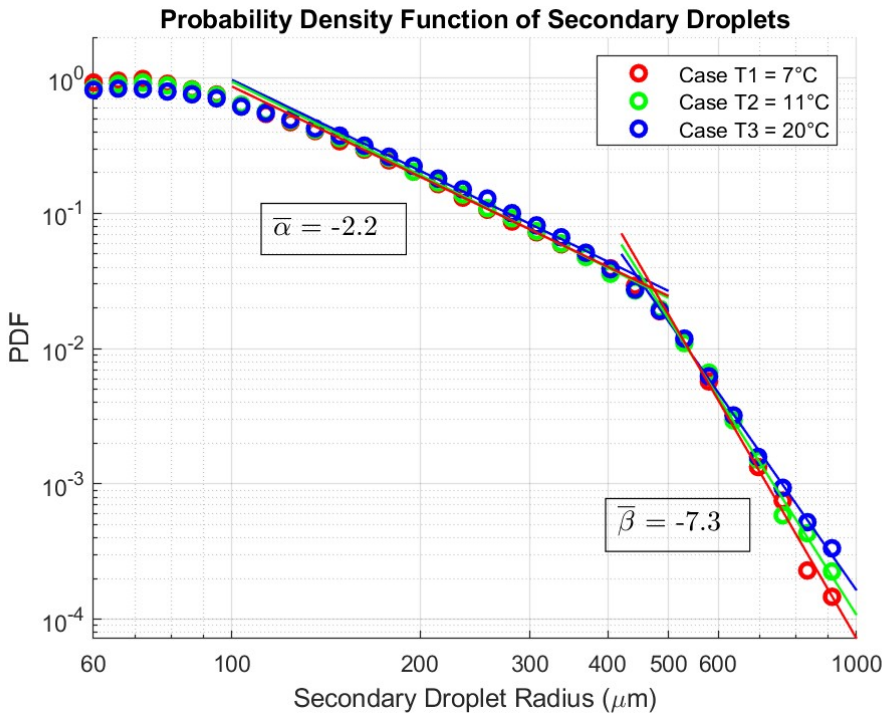

Figure 3.5: PDF of Radii in log-log Scale

be seen in the average size of secondary droplets in Figure 3.3, the average radius of the droplets increases as the raindrop temperature increases, however, the change is fairly small comparing to the droplet number. This indicates that a change in raindrop viscosity has a small affect on the composition of generated secondary droplets.

It it shown that most differences are at $60\mu m < R < 200\mu m$, so Figure 3.4b shows a detailed line plot of PDF focused on $60\mu m < R < 200\mu m$. Raindrops with lower temperature generates more smaller secondary droplets, and fewer larger secondary droplets.

It is also discovered that the radius probability distribution curve follows a power law in two regions: $100\mu m < R < 300\mu m$ and $300\mu m < R < 600\mu m$ with coefficients of $\overline{\alpha} = -2.2$ and $\overline{\beta} = -7.3$ (more detailed data is shown in Table 3.3). This figure provides an estimation of the radius profile of generated secondary droplets in a rain field.

Variable	case T1	case T2	case T3
α	-2.21	-2.29	-2.23
β	-7.95	-7.27	-6.60
$r_i(\mu m)$	473.2	465.5	444.1

Table 3.2: Coefficients of power law regions

3.2.2.3 Droplet Volume

Furthermore, the volume of the secondary droplets are calculated by using the radius information, assuming most of the droplets are spherical. A dimensionless volume V^* is calculated by equation:

$$V^* = \frac{V_{droplet}}{V_{raindrop}} \tag{3.3}$$

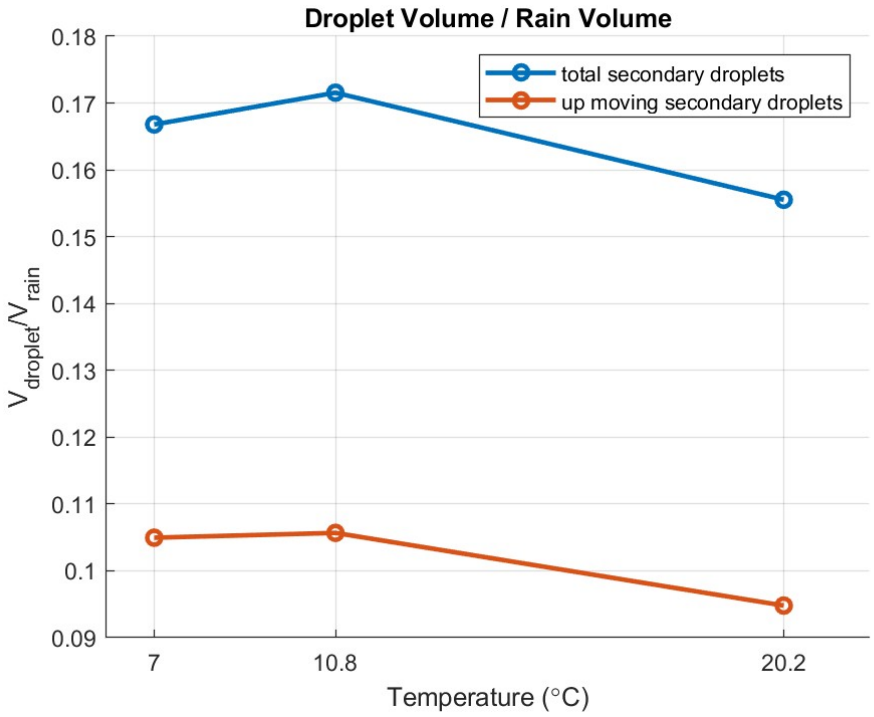

Figure 3.6: Droplet Volume per Rain Volume

It is shown that the volume of total secondary droplets is about 1.7 times larger than the produced secondary droplet. Also, the two curves follow a similar trend. Figure 3.6 shows slight change in this dimensionless volume while changing the rain temperature (less than 10%). However, the number of produced secondary droplet per raindrop decreased with increasing temperature (Figure 3.2). Hereby we could conclude that more larger droplets are produced for the low temperature case.

3.2.2.4 Droplet Kinetic Energy

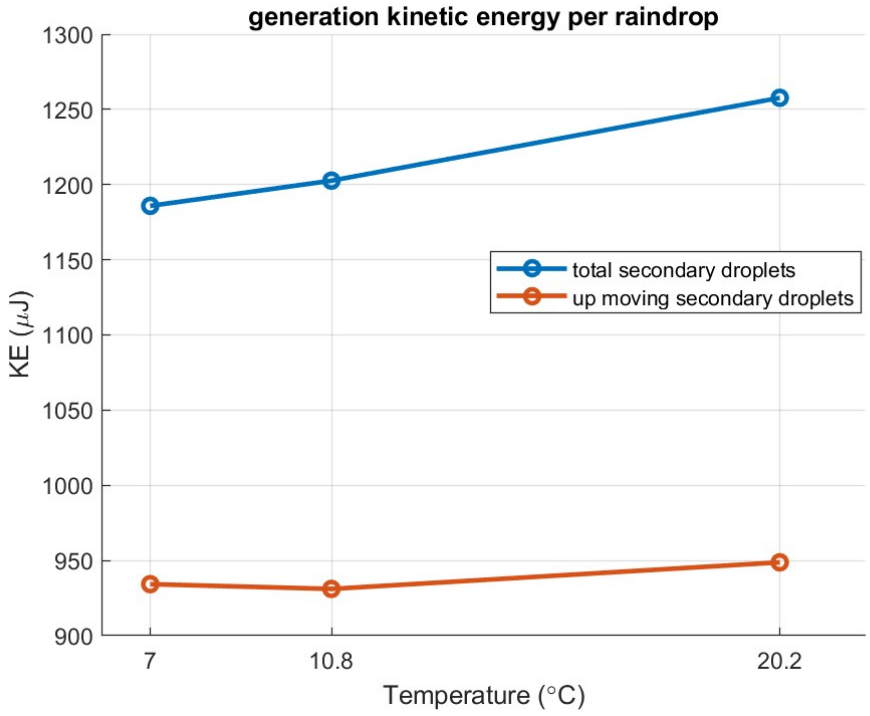

Figure 3.7: 2-D KE per Raindrop KE

Two dimensional kinetic energy is calculated by using horizontal and vertical velocity. Due to the large reconstruction error on z velocity, the reported data only includes 2 dimensional velocity. Figure 3.7 shows 2-D kinetic energy of droplets divided by the 2-D kinetic energy of

the raindrops. And it is shown that at least 10% of the energy is transferred in terms of velocity. This is a lower bound estimation because there might be larger and slower droplets that are never caught by the camera at the height of 3.75 inch. However, it is possible to produce that part of the data if we process further from the raw data. Also, by decreasing the rain temperature, the 2-D kinetic energy increases for more than 20%.

3.2.3 Summary of Rain Temperature Effect

Concluding from this past section, by changing the temperature of the rain, it is possible to change the rain rate by at least 40%, in the mean time, the total production number of secondary droplet does not change very much, resulting a significant change in the production per raindrop. Changing rain temperature has limited effect on the composition of the size of the secondary droplets, the dimensionless volume, and the dimensionless 2-D kinetic energy.

3.3 Target Pool Surface Tension Effect

3.3.1 Generated Rain Field

While the depth of the water inside the rain generator and the specification of the needles are the same throughout the experiment, it is expected that the characteristics of the rain field does not vary in this set of experiments. As shown in Figure 3.8a, the radius of the raindrops does not change much. The average radius of the raindrops is $\overline{R} = 1.42mm$ and the standard deviation is $SD = 0.01mm$. The average raindrop velocity is $\overline{V}_{rain} = 5.56m/s$, with a standard deviation of $SD = 0.02m/s$. Data shows that the radius and the velocity of the raindrop varies less than 2% throughout the surface tension experiment. Figure 3.8b shows an average of number

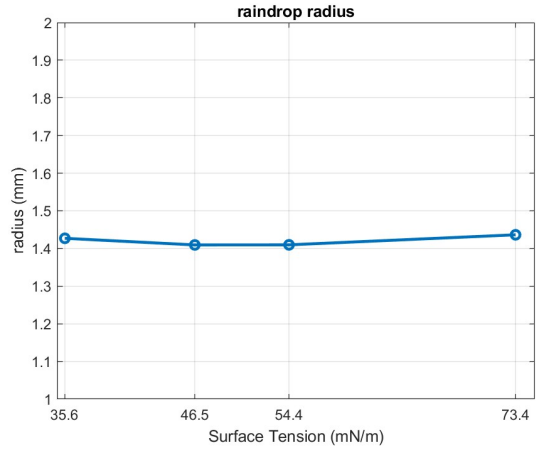

(a) Raindrop Radius

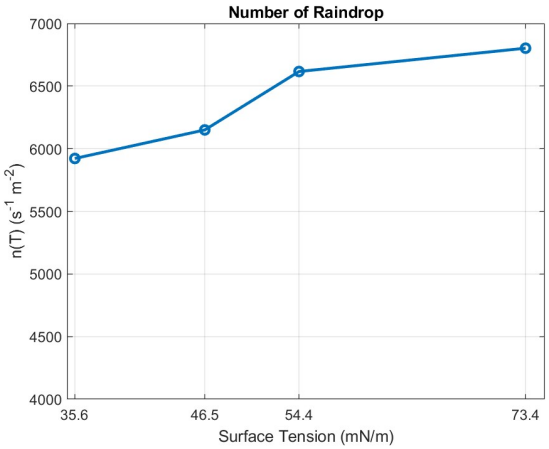

(b) Raindrop Number

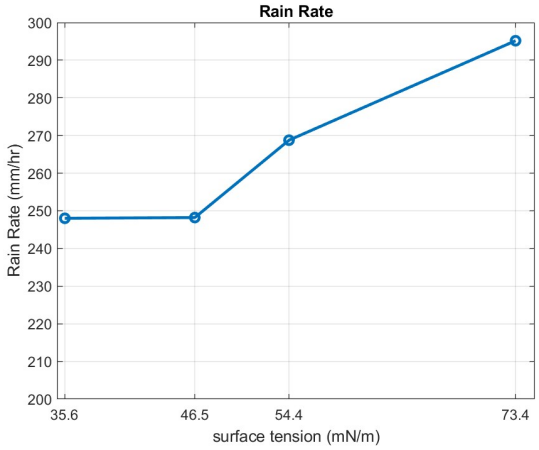

(c) Rain Rate

Figure 3.8: Rain field specifications in surface tension experiment.

of raindrops variation during the experiment, and we could see a 10% variation in the raindrop number. Figure 3.8c shows the calculated rain rate in for the three different cases.

3.3.2 Secondary Droplet

3.3.2.1 Droplet Number

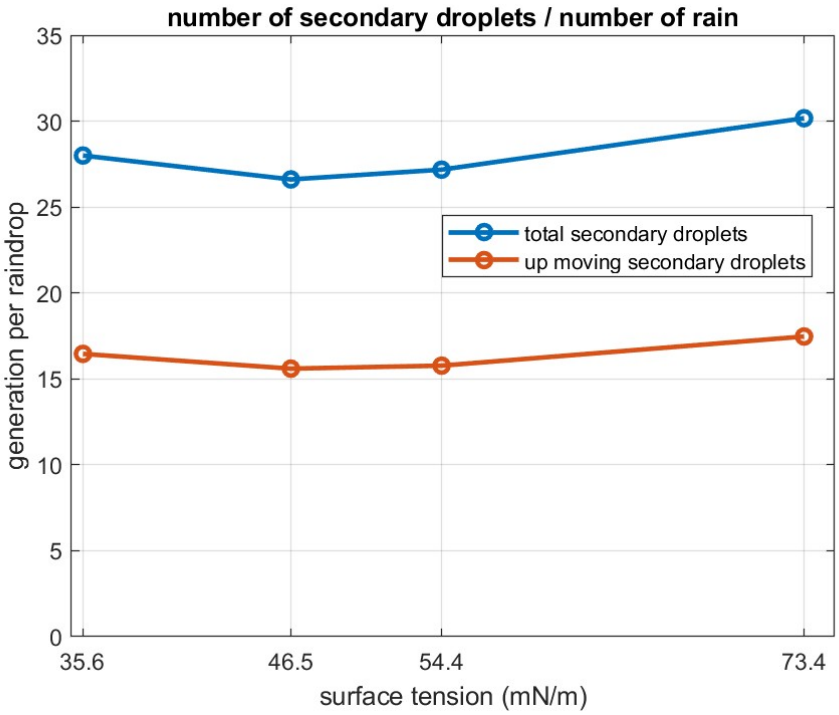

Figure 3.9: Secondary Droplet Production per Rain Drop

Figure 3.9 shows the change in number of secondary droplets per raindrop versus changing surface tension in the target pool. The total droplet line is the total number of droplet that we are able to track, and the generation line is the total number of up going droplet through the movie time range divided by the number of raindrop for every run, then average over 3 runs for each case. Two lines has very similar tendency while the number of generation is about half of the

total number of droplets.

We could see that at this height, the number of droplets decreases initially as more surfactant is added in the water (resulting a smaller surface tension value). When the surfactant concentration is approaching CMC, the number of secondary droplets increases again. However, the change is fairly small comparing with the temperature case. After examining closely, the number only changes for less than 10%. Comparing to the temperature case, it is possible to conclude that the target pool surface tension has limited effect on the number of secondary droplets at the height of 3.75 inch.

3.3.2.2 Droplet Size

Figure 3.10 shows an average droplet radius versus target pool surface tension, the average radius of the secondary droplets also follows a similar trend as the droplet production number per rain drop (Figure 3.9). Similar to the temperature case, the average radius of total droplets is smaller than the average radius of the produced droplets because smaller drops are more likely to achieve higher distance and appear on the frame.

Figure 3.11 shows a probability distribution of the radii of the secondary droplets with different scales. Figure 3.11a shows a bar plot of the secondary droplet radius distribution. Similar to the temperature cases, the difference is observed mostly in region $60\mu m < R < 100\mu m$, and it is discovered that the difference is more dramatic for the surfactant experiments.

To better see the difference, Figure 3.11b is a line plot of the PDF in the region. As the concentration of surfactant increases, a peak appears around $R = 200\mu m$ and a valley appears around $R = 90\mu m$, which does not seems to be the case when changing the rain temperature.

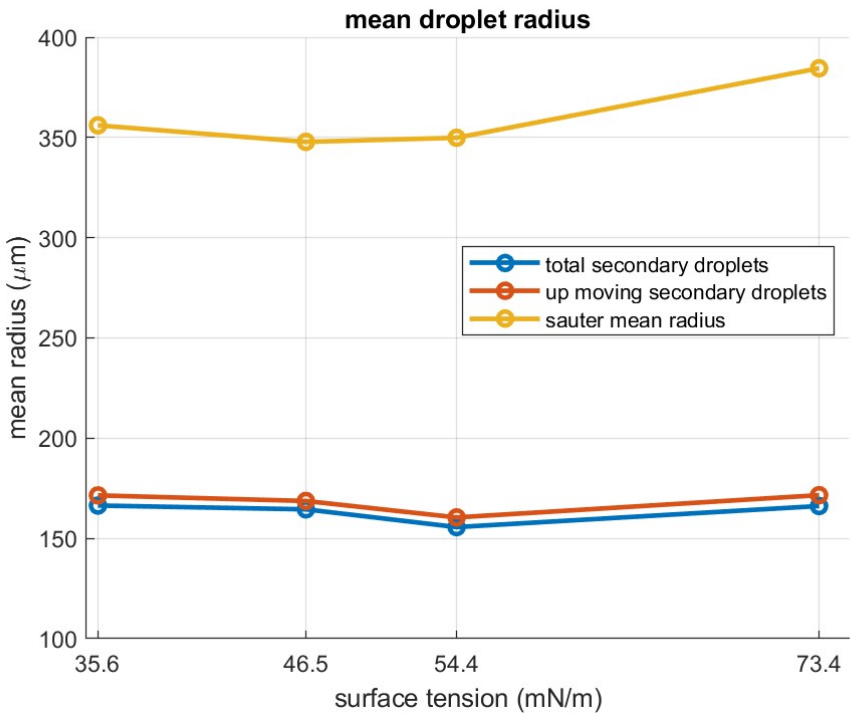

Figure 3.10: Secondary Droplet Radius

While the total number of produced secondary droplets does not change much (Figure 3.9), a possible hypothesis is that as more surfactant is added into the water, more larger droplets are produced and less smaller droplets are produced. Comparing to the clean water case, the peak and the valley in the most extreme cases changed over 20% from the clean water case.

Similar to the rain temperature cases, two power law lines were fitted to the log-log plot, with coefficients $\overline{\alpha} = -2.2$ and $\overline{\beta} = -6.3$. The coefficient in α region is very close to the temperature case which means no or limited difference on droplets with $100\mu m < R < 300\mu m$. However, region β for the surface tension case has a slightly higher slope than the temperature case.

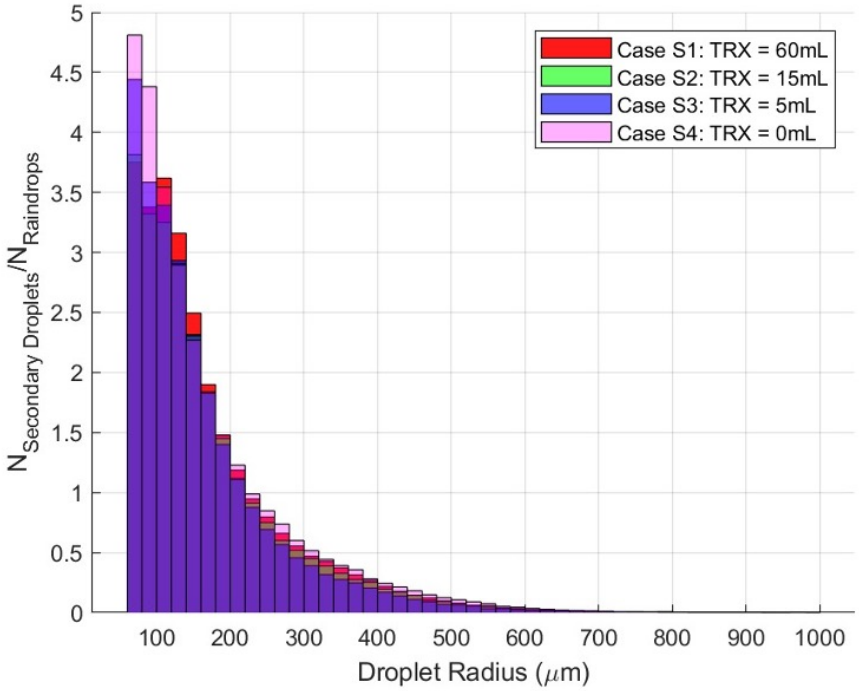

(a) Barplot

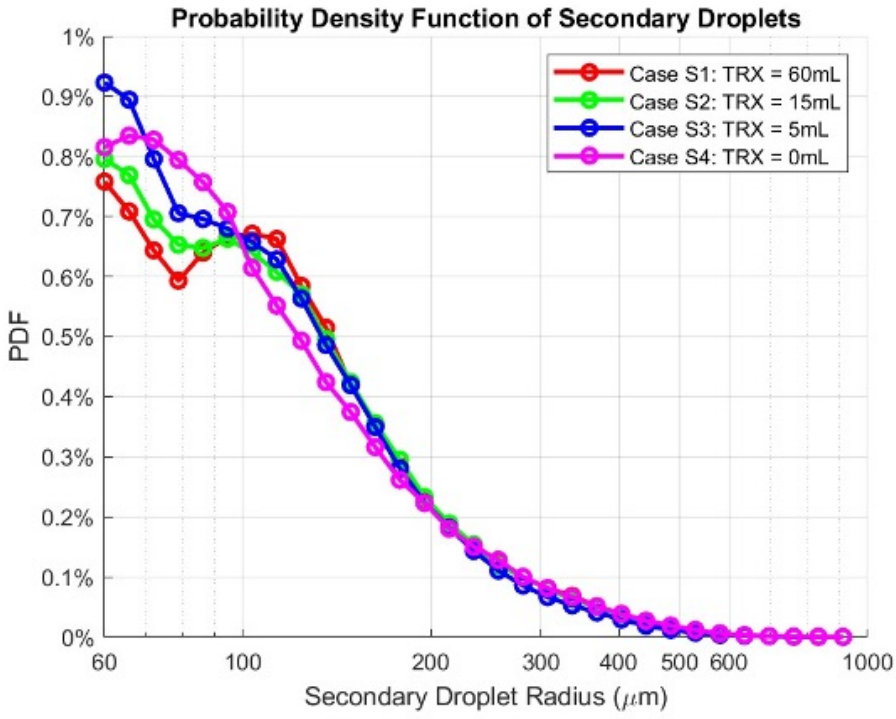

(b) Linear-Linear Plot for $60 < R < 200\mu m$

Figure 3.11: Radius Distribution of Secondary Droplets

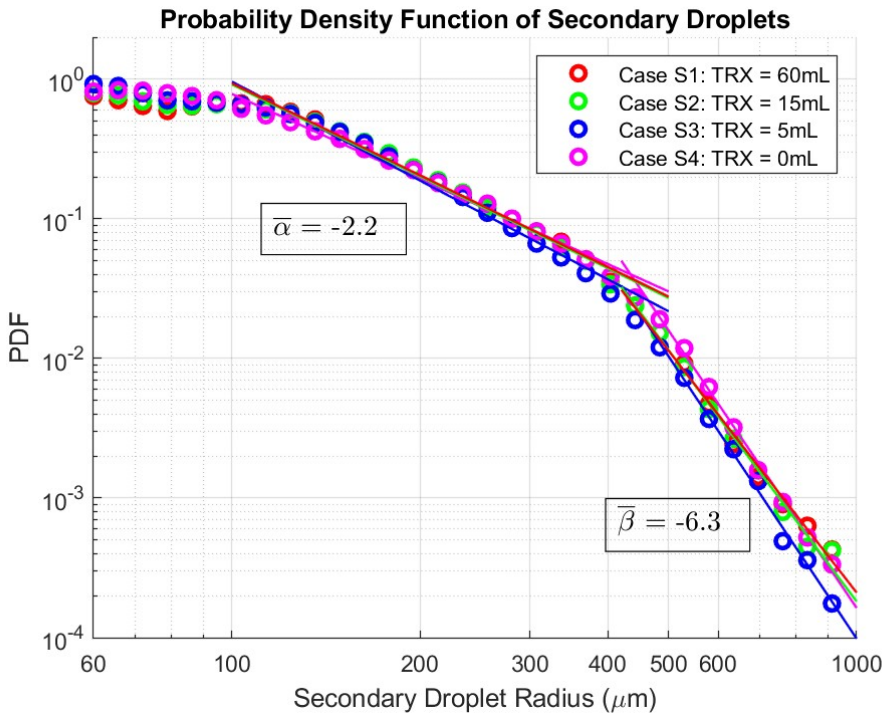

Figure 3.12: PDF of Radii in log-log Scale

Variable	case S1	case S2	case S3	case S4
α	-2.18	-2.19	-2.35	-2.02
β	-5.75	-5.98	-6.71	-6.60
$r_i(\mu m)$	389.03	398.04	421.48	434.07

Table 3.3: Coefficients of power law regions

3.3.2.3 Secondary Droplet Volume

The dimensionless volume changes from 0.095 to 0.071 and back to 0.084 as the concentration of surfactant increases which creates more than 30% change in the production. Figure 3.13 shows a similar tendency as the number and the radius plot because the volume should change simultaneously with the number and the radius of the secondary droplets. Also, the figure shows that only about 7-9% of the volume was produced and could achieve the height of 3.75 inch.

Moreover, similar to the droplet number, the total droplet volume is about two times larger than the produced droplet volume.

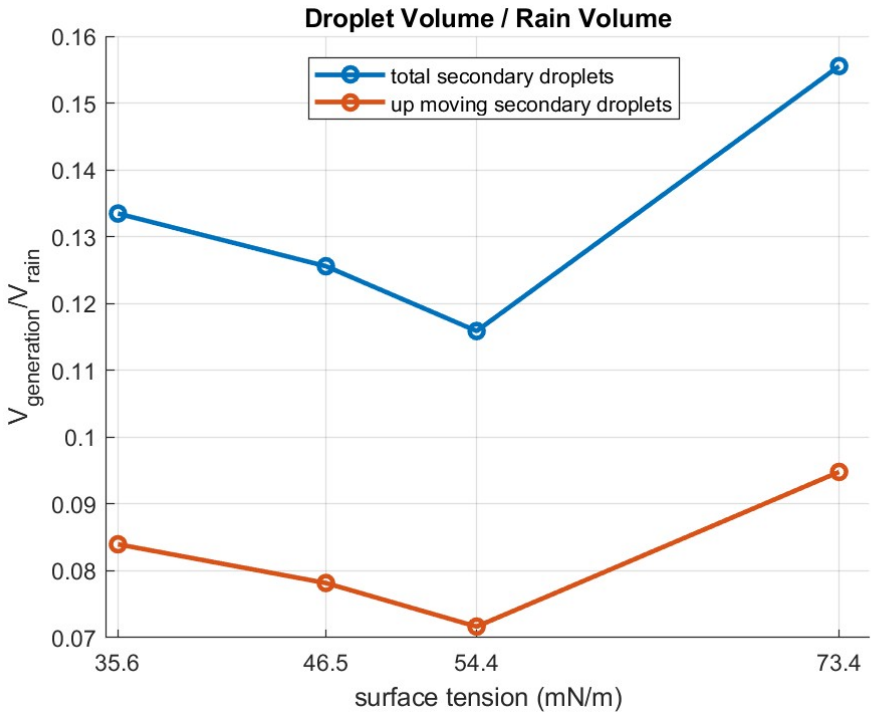

Figure 3.13: Production Volume per Rain Volume

3.3.2.4 Secondary Droplet Kinetic Energy

Two dimensional secondary droplet kinetic energy is calculated by using the radius, density and the velocity of each individual droplets. This total 2-D kinetic energy is then divided by the total raindrop kinetic energy to product the plot. the third dimension velocity is unclear since the measurement reconstruction technique is not trust worthy yet. Similar trend appears again, showing that the by changing the surface tension level, the 2-D production kinetic energy can be changed by over 35%. This can be an estimation of the total kinetic energy since the z velocity should be normally distributed and with the same tendency.

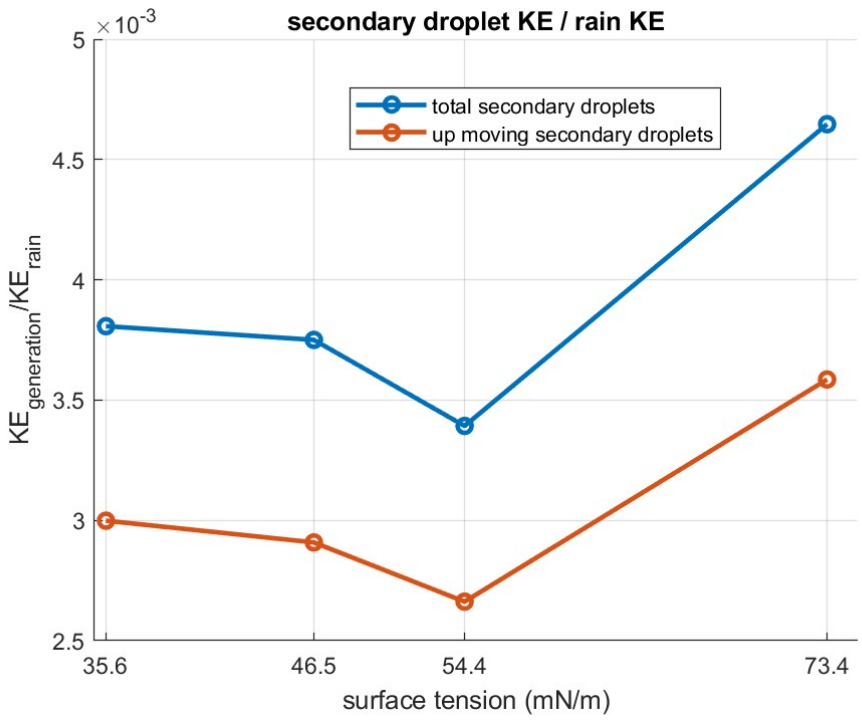

Figure 3.14: 2-D KE per Raindrop KE

3.3.3 Summary of Surface Tension Effect

It is shown that under the same rain condition, by changing the surface tension, the number, size and the 2-D kinetic energy could be changed simultaneously. They all show a ”U” shaped curve, meaning they all decrease when initially add in surfactant, then everything increases again as the surfactant level near CMC. It is also shown that as we increase the surfactant level, secondary droplets that has specific sizes are generated more than clean water, and some drops are generated less. There might be more unknown effect at the height of 2.75 and 1.75 inches above the water surface. Further research is required to understand the physical mechanism.

3.4 Additional Validation Experiments for Surface Tension Cases

Due to large variation in the rain rate for the surface tension experiments, it is needed to validate the generated rain field to eliminate time-dependent factors. Additional experiments were performed with four different surface tension levels, and one run from each cases is plotted against the original data to compare the results.

3.4.1 Generated Rain Field

Figure 3.15 shows plots of the rain specifications with additional experiments plotted as dashed lines. It is shown on Figure 3.15a that the average radius of the rain drops is stable, however, the overall average radius is about 10% larger than the original data. The total number of raindrops is significantly larger than the original data, but similar variation still exists. It is suspected that there is a large time scale in the rain rate and the data taken might not be enough for us to get a stable result. The rain rate from the additional runs is more stable than the original experiments.

Normalized secondary droplet number is shown in Figure 3.16. Dashed lines are results from additional validation experiments. It is shown that the difference is small between the original data and the additional data.

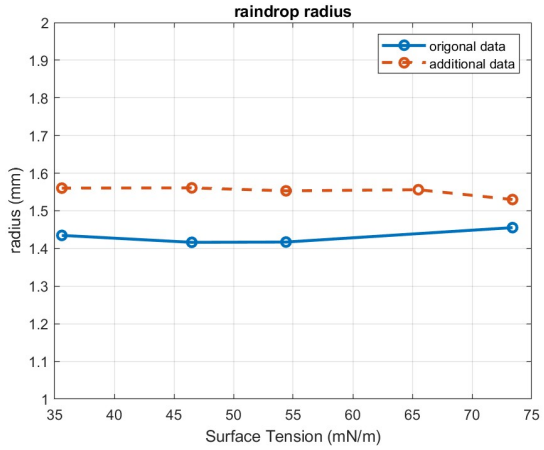

(a) Raindrop Radius

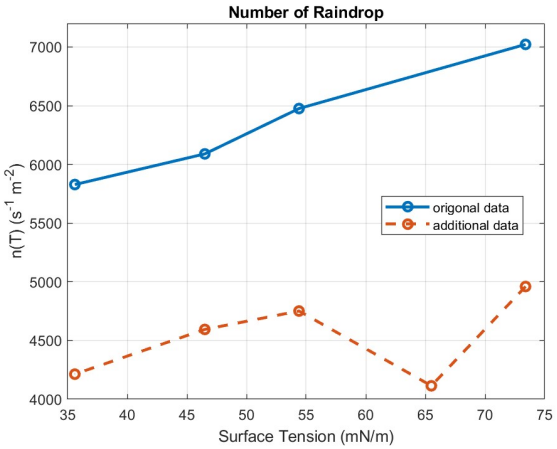

(b) Raindrop Number

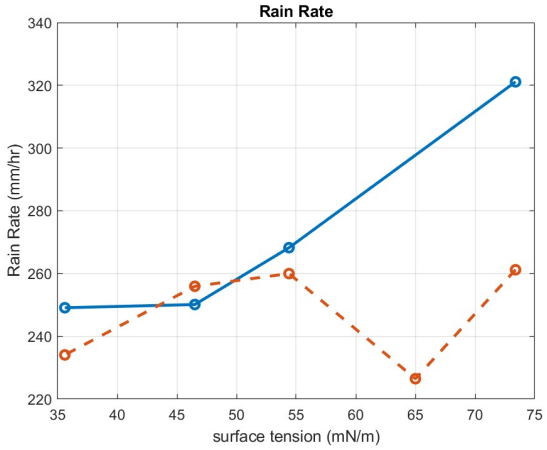

(c) Rain Rate

Figure 3.15: Rain Field Specifications Including Additional Experiments

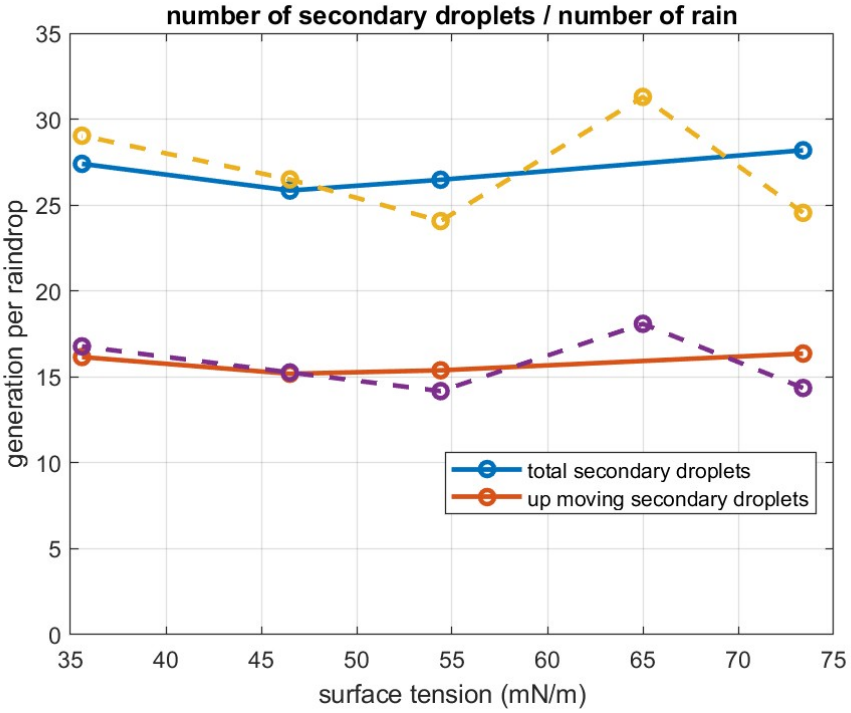

Figure 3.16: Secondary Droplet Production per Rain Drop

Chapter 4: Summary and Future Work

4.1 Summary

In this thesis, statistical data at 3.75 inch above the surface on secondary droplet production from raindrop impacting a deep water pool is reported. The impacting Weber number of the raindrops is between 1201 and 2441 depending on the case. It is found that both rain temperature and the pool surface tension has effect on the secondary droplet production. Two power law parameters has been found for both the temperature case and the surface tension case. It has been shown that the temperature of the rain could effect the production of the secondary droplet by over 50%. It is shown that the rain temperature has limited effect on the average droplet size and the droplet size distribution. The surface tension of the target pool has visible impact on the distribution of the secondary droplet size. The generation of secondary droplets that has size of $R = 90\mu m$ is limited and $R = 200\mu m$ droplets are enhanced. A "U" shaped trend is found in the average radius, number of production, and volume of production of the secondary droplets.

4.2 Future Works

First, It is shown that as we change the rain temperature, the rain rate changes accordingly. More experiment is needed to determine if the rain temperature alone has any effect on the

secondary droplet generation by keeping the rain rate constant. Second, more data processing is needed to explore the unknown data at the lower heights to get quantitative results on the effects. Finally, the reconstruction of the in-line holographic data needs more development to extract the z data so that we could have a complete data on velocity and energy.

Bibliography

[1] Fabrice Veron, *Ocean spray.* (Annual Review of Fluid Mechanics, 2015), 47(1):507–538. doi: 10.1146/annurev-fluid-010814-014651.

[2] Jin Wu, *Spray in the atmospheric surface layer: Laboratory study.* (Journal of Geophysical Research (1896-1977)), 78(3):511–519, 1973. doi: 10.1029/ JC078i003p00511. URL https://agupubs.onlinelibrary.wiley.com/doi/ abs/10.1029/JC078i003p00511.

[3] C. D. O'Dowd and G. de Leeuw, *Marine aerosol production: a review of the current knowledge.* (Philosophical Transactions of the Royal Society A: Mathematical, Physical and Engineering Sciences, 2007), 365(1856): 1753–1774.

[4] L. Bianco, J.-W. Bao, C. W. Fairall, and S. A. Michelson, *Impact of sea-spray on the atmospheric surface layer* (Boundary-Layer Meteorology, 2011) 140(3):361, doi: 10.1007/s10546-011-9617-1.

[5] Edgar L. Andreas and Kerry A. Emanuel, *Effects of sea spray on tropical cyclone intensity* (Journal of the Atmospheric Sciences, 2001) 58(24):3741–3751, doi: 10.1175/1520-0469(2001)058⟨3741:EOSSOT⟩2.0.CO;2.

[6] Y. Q. Wang, J. D. Kepert, and G. J. Holland, *The effect of sea spray evaporation on tropical cyclone boundary layer structure and intensity* (Monthly Weather Review, 2001) 129(10):2481–2500.

[7] J. Simpson, C. Kummerow, W. -K. Tao, and R. F. Adler, *On the Tropical Rainfall Measuring Mission (TRMM)* (Meteorology and Atmospheric physics, 1996), 60: 19-36.

[8] C. Kummerow, W. Barnes, T. Kozu, J. Shiue, and J. Simpson, *The Tropical Rainfall Measuring Mission (TRMM) Sensor Package* (Journal of Atmospheric and Oceanic Technology, 1997), Vol. 15, pp. 809 - 817.

[9] C. J. Zappa, D. T. Ho, W. R. McGillis, M.L. Banner, J. W. H. Dacey, L. F. Bliven, B. Ma, J. Nystuen, *Rain-induced turbulence and air-sea gas transfer* (Journal of Geophysical Research, 2009), Vol. 114.

[10] D. Atlas, *Footprints of storms on the sea: A view from spaceborne synthetic aperture radar* (Geophys. Res., 1994), 99(C4), 7961– 7969, doi:10.1029/94JC00250.

[11] Werner Alpers and Christian Melsheimer, *Rainfall* (Synthetic Aperture Radar Marine Users Manual, 2004), 353-372.

[12] I.-I. Lin, W. Alpers, V. Khoo, H. Lim, T. K. Lim and D. Kasilingam, *An ERS-1 synthetic aperture radar image of a tropical squall line compared with weather radar data* (IEEE Transactions on Geoscience and Remote Sensing, 2001), vol. 39, no. 5, pp. 937-945, doi: 10.1109/36.921411.

[13] J. Bao, C. W. Fairall, S. A. Michelson, and L. Bianco, *Parameterizations of Sea-Spray Impact on the Air–Sea Momentum and Heat Fluxes* (Mon. Wea. Rev., 2011), 139, 3781–3797, https://doi.org/10.1175/MWR-D-11-00007.1.

[14] D. C. Blanchard and L. D. Syzdek, *Concentration of bacteria in jet drops from bursting bubbles* (Journal of Geophysical Research, 1972), 77(27):5087–5099.

[15] A. R. Ravishankara, *Heterogeneous and multiphase chemistry in the troposphere* (Science, 1997), 276(5315):1058–1065.

[16] O. Reynolds, *On the floating of drops on the surface of water depending only on the purity of the surface* (Proc. Manchester Lit. Phil. Soc., 1881), Vol. 21, pp. 1 - 2.

[17] A.M. Worthington, *A Study of Splashes* (Longmans, Green, and Co, 1908).

[18] Martin Rein, *Phenomena of liquid drop impact on solid and liquid surfaces* (Fluids Dyn. Res., 1993), Vol. 12, pp. 61 - 93.

[19] C. D. Stow and R. D. Stainer, *The Physical Products of a Splashing Water Drop* (Journal of the Meteorological Society of Japan, 1977) Vol. 55, No. 5.

[20] Jie Liu, Henry Vu, Sam S. Yoon, Richard Jepsen, and Guillermo Aguilar1, *SPLASHING PHENOMENA DURING LIQUID DROPLET IMPACT* (Atomization and Sprays, 2010) 20(4), 297–310.

[21] S. K. Alghoul, C. N. Eastwick, and D. B. Hann, *Normal droplet impact on horizontal moving films: an investigation of impact behaviour and regimes* (Exp. Fluids, 2011), Vol. 50, pp. 1305 - 1316.

[22] R. M. Schotland, *Experimental results relating to the coalescence of water drops with water surfaces* (Disc. Faraday Soc., 1960), Vol. 30, pp. 72 - 77.

[23] O. W. Jayaratne and B. J. Masion, *The coalescence and bouncing of water drops at an air/water interface* (Proc. R. Soc., 1964), Vol. 280, No. 1383, pp. 545 - 565.

[24] G. L. Siscoe and Z. Levin, *Water-Drop-Surface-Wave Interactions* (Journal of Geophysical Research, 1971). Vol. 76, No. 21, pp. 5112 - 5116.

[25] L. B. Wetzel, *On the theory of electromagnetic scattering from a raindrop splash* (Radio Science, 1990), Vol. 25, pp. 1183 - 1197.

[26] D. Houk and T. Green, *A note on surface waves due to rain* (Journal of Geo- physical Research, 1976), Vol. 81, No. 24, pp. 4482 - 4484.

[27] L.F. Bliven, P. W. Sobieski, and C. Craeye, *Rain generated ring-waves: Mea- surements and modelling for remote sensing* (Int. J. Remote Sensing, 1997), Vol. 18, No. 1, pp. 221 - 228.

[28] Daniel R. Guildenbecher, Jian Gao, Phillip L. Reu, and Jun Chen, *Digital holography simulations and experiments to quantify the accuracy of 3D particle location and 2D sizing using a proposed hybrid method* (Appl. Opt., 2013), 52, 3790-3801

[29] Joseph Katz and Jian Sheng, *Applications of holography in fluid mechanics and particle dynamics* (Annual Review of Fluid Mechanics, 2010) 42(1):531–555. doi: 10.1146/annurev-fluid-121108-145508.

[30] Ren Liu, *An Experimental Study of Water Surface Features in Response to Rain* (UMD Theses and Dissertations Mechanical Engineering Theses and Dissertations, 2017), doi: https://doi.org/10.13016/M27G3S.

[31] Biolin Scientific, *Figure From Website*, https://www.biolinscientific.com/ksvnima